日本磁気学会
ISSN 1882-2924
Journal of the Magnetics Society of Japan
Electronic Journal URL: https://www.jstage.jst.go.jp/browse/msjmag

Vol.40 No.5　2016

Journal

Thin Films, Fine Particles, Multilayers, Superlattices

JOURNAL OF THE MAGNETICS SOCIETY OF JAPAN

Vol.40 No.5 2016

日本磁気学会

ISSN 1882-2924

HP: http://www.magnetics.jp/ e-mail: msj@bj.wakwak.com

Electronic Journal: http://www.jstage.jst.go.jp/browse/msjmag

有限要素法解析ソフトウェア COMSOL Multiphysics®

COMSOL MULTIPHYSICS®

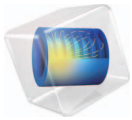

マルチフィジックスの進化論

無制限・強連成で実現象に即したシミュレーション事例のご紹介

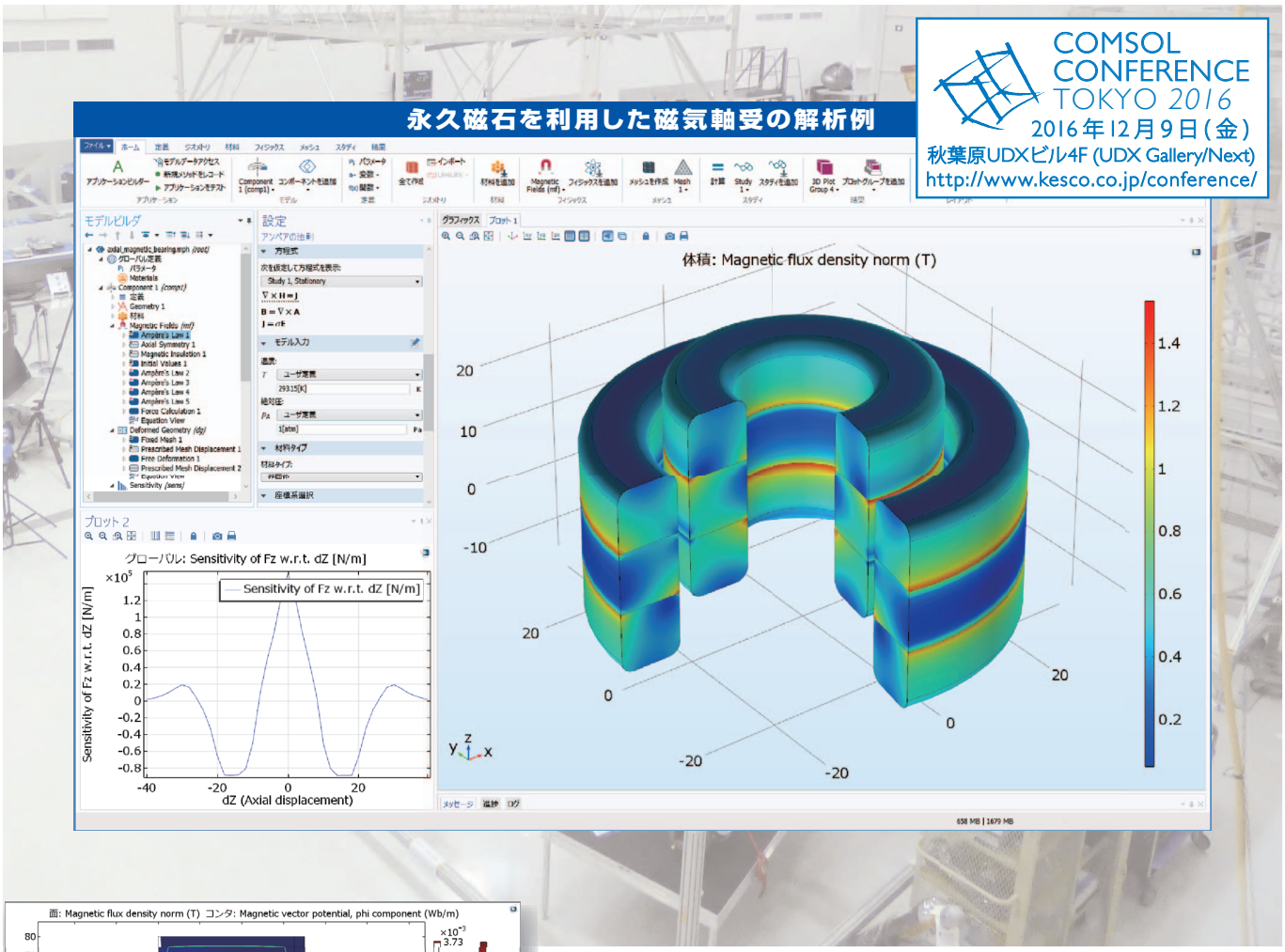

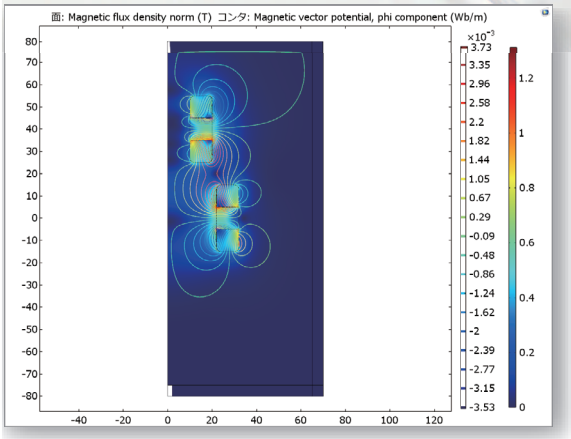

永久磁石を使用した磁気軸受

永久磁石を使用した軸受はターボ機械、ポンプ、モータ、発電機やフライホイール式エネルギー貯蔵システムなど、様々な分野で使用されています。非接触かつ潤滑不要で保守整備を大幅に省略できる点は、従来の機械式ベアリングと比べて重要なメリットです。
この例では、軸方向の永久磁石軸受の磁気力と剛性などの設計パラメータを計算する方法を示しています。

※AC/DCモジュールはCOMSOL Multiphysicsと併用するアドオン製品です。

AC/DC モジュールの適用例

- AC/DC 電流分布、電場分布
- バイオヒーティング
- コイルとソレノイド
- SPICE 回路とフィールドシミュレーション
- 接触抵抗
- 電磁両立性 (EMC) および電磁妨害 (EMI)
- 電磁力およびトルク
- 電磁力シールド
- 電気機械の変形
- ホール効果を利用したセンサ
- インシュレータ、コンデンサ、誘電体
- モータ、ジェネレータ、および他の電気機械
- 非線形材料
- 寄生容量とインダクタンス
- 永久磁石と電磁石
- 多孔質材料
- 抵抗および誘導加熱
- センサ
- 超伝導体
- 変圧器とインダクタ

COMSOL Multiphysics® なら、今まで不可能だった 3 種以上のマルチフィジックス解析を強連成で実現できます。30 日間全機能無料トライアル、無料の導入セミナー、1000種を超える世界の様々な事例をご提供いたします。詳しくは、下記の弊社営業部までお問い合せください。

COMSOL

http://www.comsol.jp

KESCO KEISOKU ENGINEERING SYSTEM
計測エンジニアリングシステム株式会社
http://www.kesco.co.jp/comsol/
Tel : 03-5282-7040 ・ Fax : 03-5282-0808

新製品 DMD 式露光装置 PALET

PALET

リーズナブル・手頃なマスクレス露光装置登場！

※特徴

- 実験室でのフォトリソグラフィ作業を大幅に簡素化
- 最速 10 秒・最小線幅 5μm で 1×0.6mm のエリアでの一括露光が可能
- 電動ステージ（オプション）との組み合わせで 20×20mm のエリアでのつなぎ合わせ露光に対応

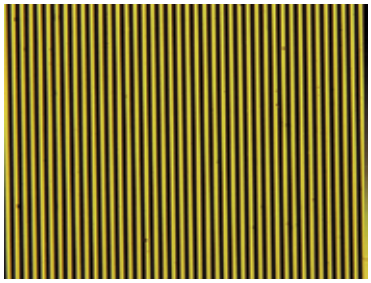

5μm 以下の
ライン & スペース

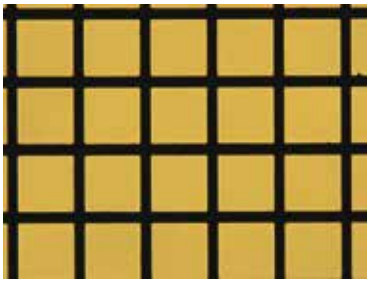

電気泳動実験用マスク

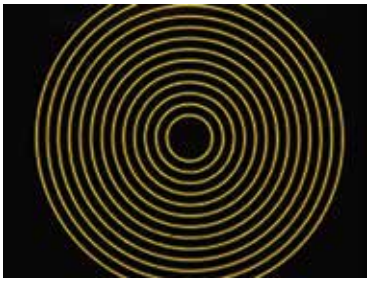

同心円パターン

新製品 特殊偏光顕微鏡（磁区観察顕微鏡）

小型でシンプル！磁区観察をより手軽に！

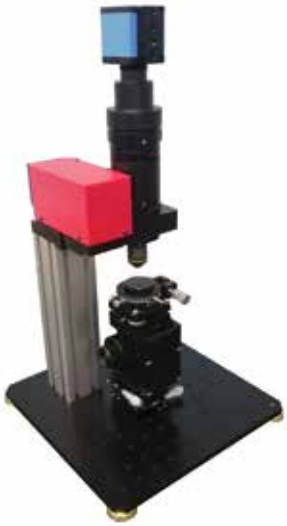

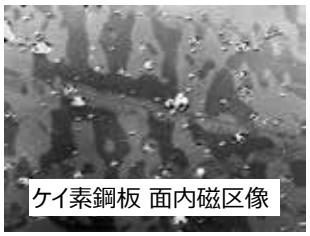

ケイ素鋼板 面内磁区像

※特徴

- 社内設計光学系による面内磁区の高コントラスト観察（空間分解能 3μm 以下 ）
- 従来機と比較し大幅の小型化
- 白色 LED 光源を用いた高安定性・長寿命

以上の製品以外に、 30 年の研究現場への対応経験に基づいた高感度・高性能の MOKE 装置、Faraday 装置、 磁区観察顕微鏡など、 各種磁気光学製品の取り揃えがございます。
お気軽にお問合せください。

レーザとレーザ応用システム製品の総合メーカー
NEOARK ネオアーク株式会社
営 業 部／〒156-0041 東京都世田谷区大原2-17-6-108 TEL(03)6379-5539 FAX(03)6379-5688
大阪支店／〒541-0056 大阪市中央区久太郎町2-3-8-201 TEL(06)6271-5123 FAX(06)6271-5110
本社 第1工場・第2工場／八王子市
URL http://www.neoark.co.jp E-mail:info@neoark.co.jp

INDEX

世界初！
高温超電導型VSM

新製品

世界初*、高温超電導マグネットをVSMに採用することで
測定速度 当社従来機1/20を実現。
0.5mm cube磁石のBr, HcJ高精度測定が可能と
なりました。
*2014年7月 東英工業調べ

測定結果例

高温超電導VSMによるNdFeB(sint.) 0.5mm cube BHカーブ

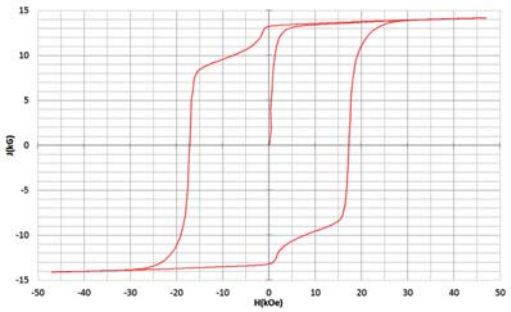

磁化測定レンジ：0.2emu
Br = 13.2kG　　HcJ = 17.2kOe

高温超電導VSMによるNdFeB(sint.) 1mm cube BHカーブ

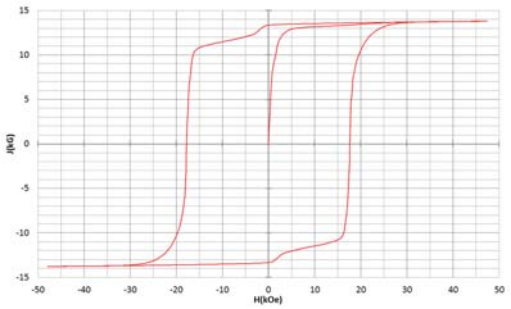

磁化測定レンジ：2emu
Br = 13.3kG　　HcJ = 17.7kOe

高温超電導VSMによるNdFeB(sint.) 4mm cube BHカーブ

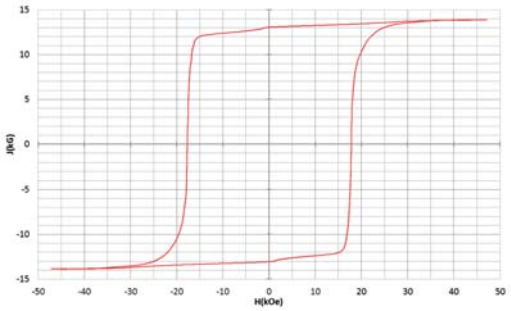

磁化測定レンジ：100emu
Br = 13.1kG　　HcJ = 17.8kOe

高速測定を実現

高温超電導マグネット採用により、高速測定を実現しました。Hmax= 5Tesla, Full Loop 測定が2分で可能です。
（当社従来機：Full Loop測定　40分）

小試料のBr,HcJ高精度測定

0.5mm cube 磁石のBr,HcJ高精度測定ができ、表面改質領域を切り出しBr,HcJの強度分布等、微小変化量の比較測定が可能です。
また、試料の加工劣化の比較測定が可能です。

試料温度可変測定

−50℃～+200℃温度可変UNIT（オプション）

磁界発生部の小型化

マグネットシステム部寸法：0.8m×0.3m×0.3m

TOEI 東英工業株式会社
http://www.toeikogyo.co.jp
〒194-0035 東京都町田市忠生1-8-13
TEL：042-791-1211 FAX：042-792-0490
E-mail : sales@toeikogyo.co.jp

Journal of the Magnetics Society of Japan
Vol. 40, No. 5

Electronic Journal URL: https://www.jstage.jst.go.jp/browse/msjmag

CONTENTS

J. Magn. Soc. Jpn., **40**, 132-136 (2016)

<Paper>

Preparation of YCo_5 and $GdCo_5$ Ordered Alloy Epitaxial Thin Films on Cu(111) Underlayer

Makoto Yamada, Yusuke Hotta, Mitsuru Ohtake,
Masaaki Futamoto, Fumiyoshi Kirino*, and Nobuyuki Inaba**

Faculty of Science and Engineering, Chuo University, *1-13-27 Kasuga, Bunkyo-ku, Tokyo 112-8551, Japan*
*Graduate School of Fine Arts, Tokyo University of the Arts, *12-8 Ueno-koen, Taito-ku, Tokyo 110-8714, Japan*
**Faculty of Engineering, Yamagata University, *4-3-16 Jyonan, Yonezawa, Yamagata 992-8510, Japan*

$Y_{17}Co_{83}$ and $Gd_{17}Co_{83}$ (at. %) alloy thin films are prepared on Cu(111) underlayers epitaxially grown on MgO(111) substrates at a substrate temperature of 500 °C by molecular beam epitaxy. The growth behavior and the film structure are investigated by *in-situ* reflection high-energy electron diffraction and X-ray diffraction. YCo_5 and $GdCo_5$ ordered alloy crystals epitaxially grow on the Cu underlayers. The epitaxial films consist of two (0001) variants whose orientations are rotated around the film normal by 30° each other. The epitaxial orientation relationships are (YCo_5 or $GdCo_5$)(0001)[$1\bar{1}00$] || Cu(111)[$11\bar{2}$] (type A) and (YCo_5 or $GdCo_5$)(0001)[$11\bar{2}0$] || Cu(111)[$11\bar{2}$] (type B). The volume ratios of two variants, $V_{\text{type A}}$: V_{typeB}, in YCo_5 and $GdCo_5$ films are estimated to be 65:35 and 72:28, respectively. The long-range order degrees of YCo_5 and $GdCo_5$ films are respectively determined to be 0.63 and 0.65. These ordered alloy films show perpendicular magnetic anisotropies reflecting the magnetocrystalline anisotropies of YCo_5 and $GdCo_5$ crystals.

Key words: YCo_5, $GdCo_5$, ordered alloy, epitaxial thin film, perpendicular magnetic anisotropy

1. Introduction

Magnetic thin films with the easy magnetization axis perpendicular to the substrate surface and with the uniaxial magnetocrystalline anisotropy energy (K_u) greater than 10^7 erg/cm^3 have been investigated for applications like future recording media with the areal density exceeding 1 Tb/in^2. A bulk $SmCo_5$ ordered alloy material with RT_5-type (*R*: rare earth metal, *T*: transition metal) structure (Fig. 1) shows K_u of 1.1×10^8 erg/cm^3 along the *c*-axis.[1] (0001)-oriented $SmCo_5$ polycrystalline[2–7] and epitaxial[8–10] films have been prepared on Cu,[2–5,8,9] Ru,[6,7,10] and Ru-Cr[7] underlayers.

The Sm and Co sites in $SmCo_5$ structure can be replaced with other *R* and *T* elements, respectively. In our previous studies, $SmFe_5$[11–13] and $SmNi_5$[11,14] ordered alloy epitaxial films were prepared on Cu(111) underlayers by using a molecular beam epitaxy (MBE) system equipped with a reflection high-energy electron diffraction (RHEED) facility. The crystallographic properties during formations of SmT_5 alloy films can be investigated by *in-situ* RHEED.

Ferromagnetic ordered alloys consisting of Co and *R* other than Sm with RT_5 structure such as YCo_5 and $GdCo_5$ also show K_u values greater than 10^7 erg/cm^3. However, there are few reports on the formations of (0001)-oriented RCo_5 epitaxial films. In the present study, $Y_{17}Co_{83}$ and $Gd_{17}Co_{83}$ (at. %) materials are deposited on Cu(111) underlayers. The growth behavior and the film structure are investigated.

2. Experimental Procedure

Thin films were deposited on polished MgO(111) single-crystal substrates by using an MBE system with the base pressure lower than 7×10^{-9} Pa. Pure Y (99.9%) and Gd (99.9%) metals were evaporated by electron beam heating, while pure Co (99.9%) and Cu (99.9999%) materials were evaporated by using Knudsen cells.

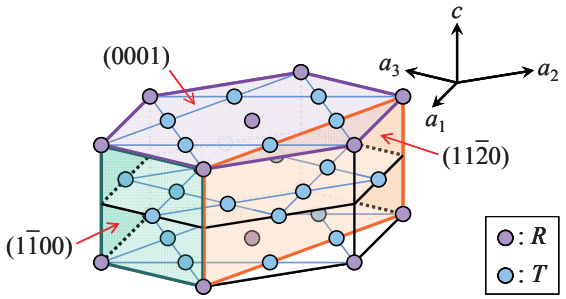

Fig. 1 Schematic diagram of RT_5 structure.

The film layer structures were $Y_{17}Co_{83}$(20 nm) /Cu(20 nm)/MgO(111) and $Gd_{17}Co_{83}$(20 nm)/Cu(20 nm) /MgO(111). MgO substrates were heated at 500 °C for 1 hour before film formation to obtain clean surfaces. 20-nm-thick Cu underlayers were deposited on the substrates. The epitaxial orientation relationships between Cu underlayer and MgO substrate were Cu(111)[$11\bar{2}$] || MgO(111)[$11\bar{2}$] and Cu(111)[$\bar{1}\bar{1}2$] || MgO(111)[$11\bar{2}$]. $Y_{17}Co_{83}$ and $Gd_{17}Co_{83}$ films of 20 nm thickness were formed by co-evaporation of Y and Co or Gd and Co materials. The film composition was confirmed by energy dispersive X-ray spectroscopy to be within 17 ± 2 at. % *R* (*R* = Y or Gd), which is nearly the RCo_5 stoichiometry. The substrate temperature during film formation was kept constant at 500 °C.

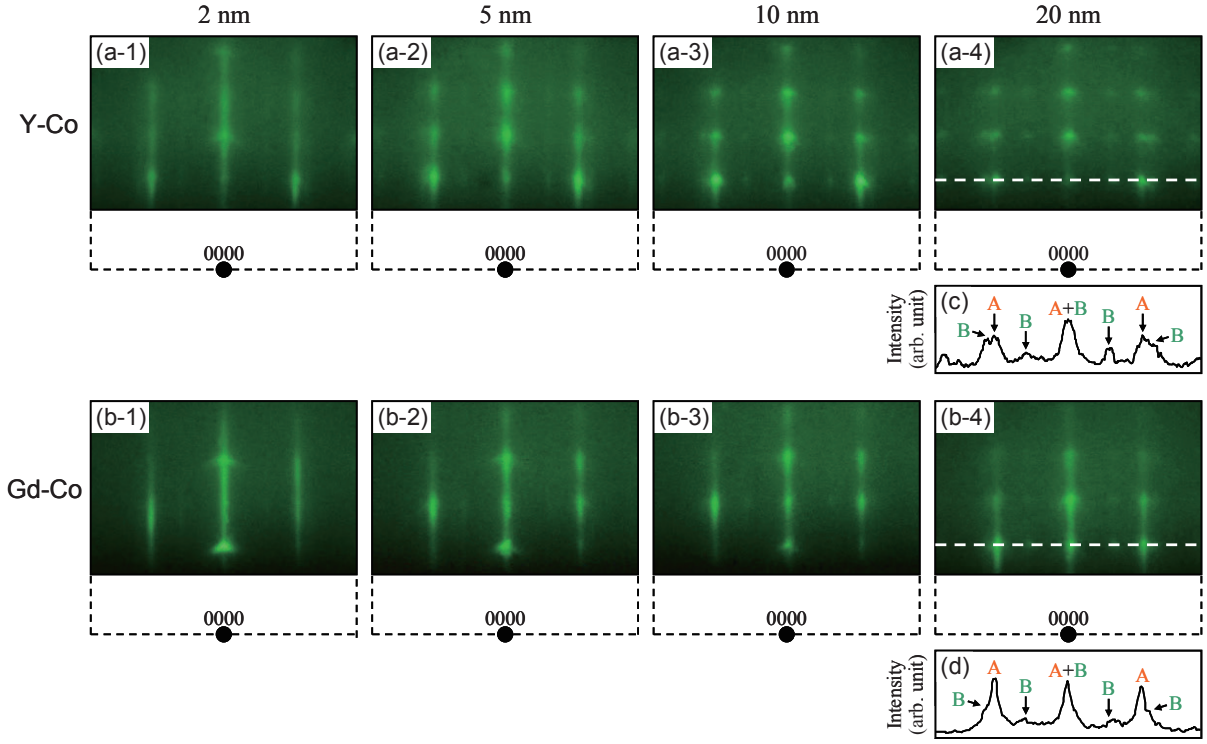

Fig. 2 [(a), (b)] RHEED patterns observed during formations of (a) $Y_{17}Co_{83}$ and (b) $Gd_{17}Co_{83}$ films on Cu(111) underlayers at 500 °C. The film thicknesses are [(a-1), (b-1)] 2, [(a-2), (b-2)] 5, [(a-3), (b-3)] 10, and [(a-4), (b-4)] 20 nm. The incident electron beam is parallel to MgO[11$\bar{2}$] (‖ Cu[11$\bar{2}$], [$\bar{1}$1$\bar{2}$]). The intensity profiles of (c) and (d) are measured along the white dotted lines in (a-4) and (b-4), respectively.

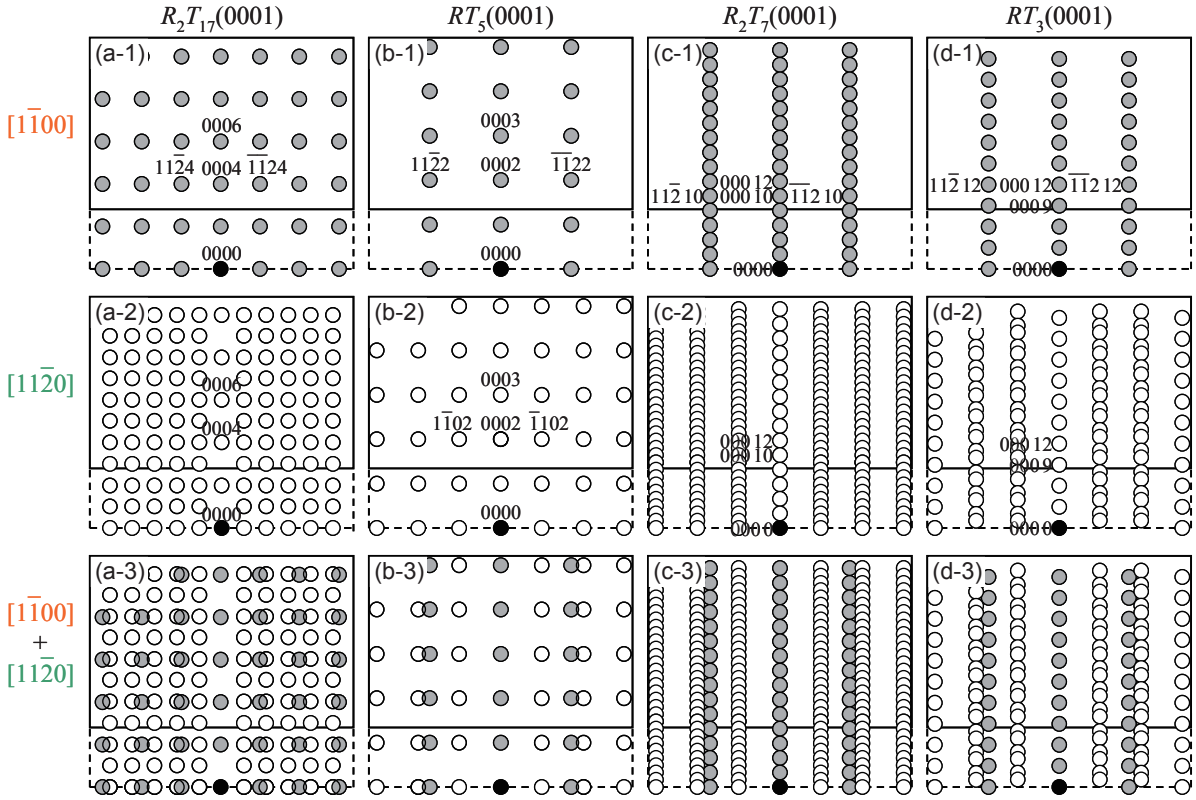

Fig. 3 [(a-1)–(d-1), (a-2)–(d-2)] Schematic diagrams of RHEED patterns simulated for hexagonal (a) R_2T_{17}, (b) RT_5, (c) R_2T_7, and (d) RT_3 ordered alloy crystals of (0001) orientation by using the lattice constants of bulk R_2T_{17} (a/2= 0.42 nm, c/2 = 0.40 nm), RT_5 (a =0.50 nm, c = 0.40 nm), R_2T_7 (a = 0.50 nm, c/9 = 0.40 nm), and RT_3 (a = 0.50 nm, c/6 = 0.40 nm) crystals. The incident electron beam is parallel to (a-1)–(d-1) [1$\bar{1}$00] or (a-2)–(d-2) [11$\bar{2}$0]. Schematic diagrams of (a-3)–(d-3) are drawn by overlapping (a-1)–(d-1) and (a-2)–(d-2), respectively.

The surface structure during film deposition was observed by RHEED. The resulting film structure was investigated by $2\theta/\omega$ scan out-of-plane, $2\theta\chi/\varphi$ scan in-plane, and β-scan pole-figure X-ray diffractions (XRDs) with Cu-Kα radiation (λ = 0.15418 nm). The magnetization curves were measured by superconducting quantum interference device (SQUID) magnetometry.

3. Results and Discussion

Figures 2(a) and (b) show the RHEED patterns of $Y_{17}Co_{83}$ and $Gd_{17}Co_{83}$ films deposited on Cu(111) underlayers observed by making the incident electron beam parallel to MgO[$11\bar{2}$] (∥ Cu[$11\bar{2}$], [$\bar{1}\bar{1}2$]). Figure 3 shows the schematic diagrams of RHEED patterns simulated for hexagonal R_2T_{17}, RT_5, R_2T_7, and RT_3 ordered crystals of (0001) orientation. A clear RHEED pattern corresponding to the diffraction pattern simulated for RT_5(0001) surface [Fig. 3(b-3)] starts to be observed from the beginning of deposition and it remains unchanged until the end of film formation for both films. $Y_{17}Co_{83}$ and $Gd_{17}Co_{83}$ epitaxial films with RT_5 ordered structure are obtained. The observed RHEED patterns are analyzed to be an overlap of two reflections, as shown by the symbols, A and B, in the RHEED intensity profiles of Figs. 2(c) and (d). The crystallographic orientation relationships are thus determined as follows,

$(YCo_5, GdCo_5)(0001)[1\bar{1}00]$ ∥ Cu(111)[$11\bar{2}$], [$\bar{1}\bar{1}2$]
∥ MgO(111)[$11\bar{2}$], (type A)

$(YCo_5, GdCo_5)(0001)[11\bar{2}0]$ ∥ Cu(111)[$11\bar{2}$], [$\bar{1}\bar{1}2$]
∥ MgO(111)[$11\bar{2}$]. (type B)

The epitaxial films consist of two types of (0001) variant whose orientations are rotated around the film normal by 30° each other, which is similar to the growth of $SmCo_5$ film on Cu(111) underlayer.[8,9]

The lattice misfit values of YCo_5 and $GdCo_5$ crystals with respect to Cu underlayer are respectively –3.4% and –2.9% in the A-type orientation relationship, whereas those are +11.5% and +12.2% in the B-type relationship. Here, the mismatches are calculated by using the lattice constants of bulk YCo_5 (a_{YCo5} = 0.4937 nm),[15] $GdCo_5$ (a_{GdCo5} = 0.4963 nm),[15] and Cu (a_{Cu} = 0.3615 nm)[16] crystals. Although there are fairly large mismatches in the cases of B-type YCo_5 and $GdCo_5$ variants, epitaxial growth is taking place. The intensity of RHEED spot from A-type variant is stronger than that from B-type variant for both materials [Figs. 2(c), (d)]. The nucleation of A-type variant with smaller lattice misfits seems to be favored.

In order to investigate the volume ratio of two types of variant, β-scan pole-figure XRD was carried out. Figure 4 shows the β-scan XRD patterns of $Y_{17}Co_{83}$ and $Gd_{17}Co_{83}$ films measured by fixing the tilt and

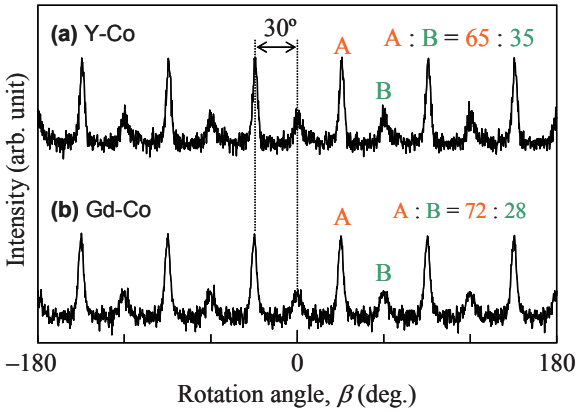

Fig. 4 β-scan pole-figure XRD patterns of (a) $Y_{17}Co_{83}$ and (b) $Gd_{17}Co_{83}$ films deposited on Cu(111) underlayers measured by fixing the (α, $2\theta B$) values at (45°, 30.5°). The intensity is shown in linear scale.

diffraction angles of (α, $2\theta B$) at (45°, 30.5°), where $YCo_5\{1\bar{1}01\}$ and $GdCo_5\{1\bar{1}01\}$ reflections are expected to be detectable. Twelve $\{1\bar{1}01\}$ reflections, which originate from the two types of variant, are observed with 30° separation for both films. The volume ratios of A-type to B-type variant in $Y_{17}Co_{83}$ and $Gd_{17}Co_{83}$ films are estimated from the integrated intensities of $\{1\bar{1}01\}$ reflections to be 65:35 and 72:28, respectively. It is revealed that the volume ratio of A-type variant is larger than that of B-type variant.

Figures 5(a-1) and (b-1) show the out-of-plane XRD patterns of $Y_{17}Co_{83}$ and $Gd_{17}Co_{83}$ films, respectively. RT_5(0001) superlattice and RT_5(0002) fundamental reflections are clearly observed for both films. The out-of-plane XRD confirms the formations of YCo_5 and $GdCo_5$ ordered phases. Long-range order degree, S, is estimated by comparing the intensities of superlattice and fundamental reflections. The intensity (I) is proportional to structure factor and the complex conjugate (FF^*), Lorentz-polarization factor (L), and absorption factor (A).[17] $F_{(0001)}$ and $F_{(0002)}$ are respectively $S(f_R - f_T)$ and $f_R + 5f_T$,[18] where f is the atomic scattering factor. Therefore, $I_{(0001)}/I_{(0002)}$ is expressed as

$$I_{RT_5(0001)}/I_{RT_5(0002)} = (FF^*LA)_{RT_5(0001)}/(FF^*LA)_{RT_5(0002)}$$
$$= S^2[(f_R - f_T)^2]_{RT_5(0001)}/[(f_R + 5f_T)^2]_{RT_5(0002)}$$
$$\times (LA)_{RT_5(0001)}/(LA)_{RT_5(0002)}. \quad (1)$$

By solving this equation, S is given as

$$S = [I_{RT_5(0001)}/I_{RT_5(0002)}]^{1/2}$$
$$\times (f_R + 5f_T)_{RT_5(0002)}/(f_R - f_T)_{RT_5(0001)}$$
$$\times [L_{RT_5(0002)}/L_{RT_5(0001)}]^{1/2}$$
$$\times [A_{RT_5(0002)}/A_{RT_5(0001)}]^{1/2}. \quad (2)$$

The S values of $Y_{17}Co_{83}$ and $Gd_{17}Co_{83}$ films are respectively calculated to be 0.63 and 0.65.

Figures 5(a-2) and (b-2) show the in-plane XRD

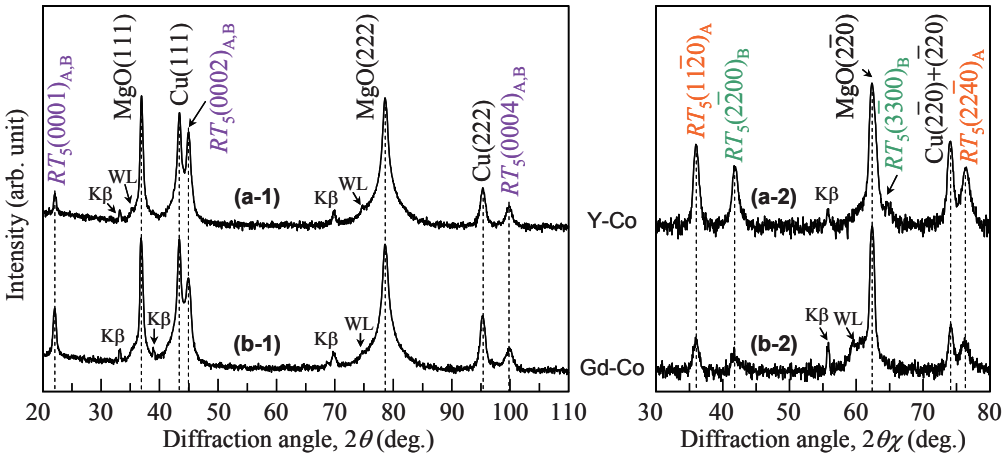

Fig. 5 [(a-1), (b-1)] Out-of-plane and [(a-2), (b-2)] in-plane XRD patterns of (a) $Y_{17}Co_{83}$ and (b) $Gd_{17}Co_{83}$ films deposited on Cu(111) underlayers. The scattering vector of in-plane XRD is parallel to MgO[1$\bar{1}$0]. The small reflections noted as Kß and WL are due to Cu-Kß and W-Lα radiations included in the X-ray source, respectively. The intensity is shown in logarithmic scale.

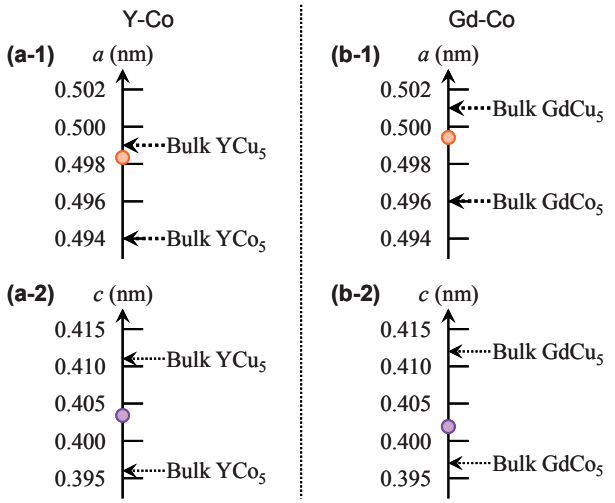

Fig. 6 Lattice constants of [(a-1), (b-1)] *a* and [(a-2), (b-2)] *c* of (a) $Y_{17}Co_{83}$ and (b) $Gd_{17}Co_{83}$ films deposited on Cu(111) underlayers.

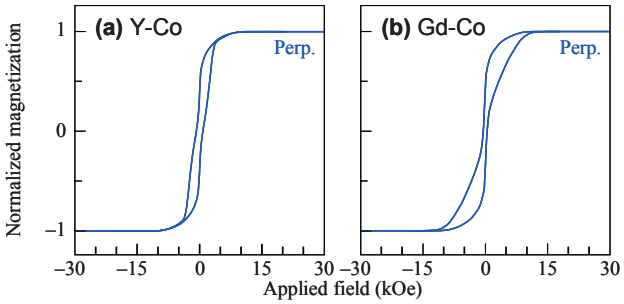

Fig. 7 Magnetization curves of (a) $Y_{17}Co_{83}$ and (b) $Gd_{17}Co_{83}$ films deposited on Cu(111) underlayers.

patterns measured by making the scattering vector parallel to MgO[1 $\bar{1}$ 0]. RT_5(11 $\bar{2}$ 0) and RT_5(22 $\bar{4}$ 0) reflections from A-type variant and RT_5(2 $\bar{2}$ 00) and RT_5(3 $\bar{3}$ 00) reflections from B-type variant are recognized for both films. The in-plane XRD confirms the epitaxial orientation relationship determined by RHEED.

Figure 6 shows the lattice constants, *a* and *c*, of $Y_{17}Co_{83}$ and $Gd_{17}Co_{83}$ films, which are respectively estimated from the peak position angles of $RT_5(22\bar{4}0)$ and RT_5(0004) reflections. Here, the lattice constants of bulk YCo_5, $GdCo_5$, $Y_{0.8}Cu_{5.4}$, and $GdCu_5$ crystals are cited from Refs. 15, 19, and 20. The *a* and *c* values of $Y_{17}Co_{83}$ and $Gd_{17}Co_{83}$ films are between those of bulk YCo_5 and $Y_{0.8}Cu_{5.4}$ crystals and between those of bulk $GdCo_5$ and $GdCu_5$ crystals, respectively. It is reported that Cu atoms of underlayer diffuse into Sm-Co film and partially substitute the Co site in $SmCo_5$ structure forming an alloy compound of $Sm(Co,Cu)_5$.[4,5] The dissolution of Cu atom into Sm-Co alloy is known to stabilize RT_5 ordered structure.[21–23] In the present case, Cu atoms are considered to have diffused from the underlayers into the $Y_{17}Co_{83}$ and $Gd_{17}Co_{83}$ films forming alloy compounds of $Y(Co,Cu)_5$ and $Gd(Co,Cu)_5$. It is necessary to confirm the element distribution by using a chemical analysis method.

Figure 7 shows the magnetization curves of $Y_{17}Co_{83}$ and $Gd_{17}Co_{83}$ films measured by applying the magnetic field along the perpendicular direction. These films are easily magnetized, which seems to be reflecting the easy magnetization axis of YCo_5 and $GdCo_5$ ordered alloy crystals.

4. Conclusion

$Y_{17}Co_{83}$ and $Gd_{17}Co_{83}$ thin films are deposited on Cu(111) underlayers at 500 °C. The film growth behavior and the detailed film structure are investigated by RHEED and XRD. YCo_5 and $GdCo_5$ ordered alloy epitaxial films of (0001) orientation are obtained. The films consist of two types of (0001) variant

whose orientations are rotated around the film normal by 30° each other. The S values of YCo_5 and $GdCo_5$ films are estimated to be 0.63 and 0.65, respectively. Cu atoms are considered to have diffused from the underlayers into the YCo_5 and $GdCo_5$ films and substitute the Co sites in YCo_5 and $GdCo_5$ structures forming alloy compounds of $Y(Co,Cu)_5$ and $Gd(Co,Cu)_5$. These ordered alloy films show perpendicular magnetic anisotropies reflecting the magnetocrystalline anisotropies of YCo_5 and $GdCo_5$ crystals.

Acknowledgments Authors thank Prof. Hirohiko Sato Chuo University for SQUID measurements. A part of this work was supported by JSPS KAKENHI Grant Numbers 25420294 and 26820117 and Chuo University Grant for Special Research.

References

1) K. J. Strnat: *Handbook of Ferromagnetic Materials* (Elsevier Science B. V., New York, 1988).
2) J. Sayama, T. Asahi, K. Mizutani, and T. Osaka: *J. Phys. D*, **37**, L1 (2004).
3) S. Takei, A. Morisako, and M. Matsumoto: *J. Magn. Magn. Mater.*, **272–276**, 1703 (2004).
4) J. Sayama, K. Mizutani, T. Ariake, K. Ouchi, and T. Osaka: *J. Magn. Magn. Mater.*, **301**, 271 (2006).
5) Y. K. Takahashi, T. Ohkubo, and K. Hono: *J. Appl. Phys.*, **100**, 053913 (2006).
6) I. Kato, S. Takei, X. Liu, and A. Morisako: *IEEE Trans. Magn.*, **42**, 2366 (2006).
7) X. Liu, H. Zhao, Y. Kubota, and J. -P. Wang: *J. Phys. D.*, **41**, 232002 (2008).
8) Y. Nukaga, M. Ohtake, F. Kirino, and M. Futamoto: *IEEE Trans. Magn.*, **44**, 2891 (2008).
9) M. Ohtake, Y. Nukaga, F. Kirino, and M. Futamoto: *J. Cryst. Growth*, **311**, 2251 (2009).
10) M. Seifert, V. Neu, and L. Schultz: *Appl. Phys. Lett.*, **94**, 022501 (2009).
11) M. Ohtake, O. Yabuhara, Y. Nukaga, F. Kirino, and M. Futamoto: *J. Appl. Phys.*, **107**, 09A708 (2010).
12) O. Yabuhara, M. Ohtake, Y. Nukaga, F. Kirino, and M. Futamoto: *J. Phys.: Conf. Ser.*, **200**, 082026 (2010).
13) T. Yanagawa, M. Ohtake, F. Kirino, and M. Futamoto: *EPJ Web Conf.*, **40**, 06007 (2013).
14) M. Yamada, Y. Hotta, T. Yanagawa, M. Ohtake, F. Kirino, and M. Futamoto: *IEEE Trans. Magn.*, **50**, 2101604 (2014).
15) H. Ido, M. Nanjo, and M. Yamada: *J. Appl. Phys.*, **75**, 7140 (1994).
16) D. N. Batchelder and R. O. Simmons: *J. Appl. Phys.*, **36**, 2864 (1965).
17) B. D. Cullity: *Elements of X-Ray Diffraction* (Addison-Wesley, Massachusetts, 1956).
18) M. Ohtake and M. Futamoto: *J. Magn. Soc. Jpn.*, **39**, 205 (2015).
19) Y. C. Chuang, C. H. Wu, and Y. C. Chang: *J. Less-Common Met.*, **84**, 201 (1982).
20) J. M. Barandiaran, D. Gignoux, J. M. Rodriguez Fernandez, and D. Schmitt: *Physica B*, **154**, 293 (1989).
21) F. Hofer: *IEEE Trans. Magn.*, **6**, 221 (1970).
22) K. Kamio, Y. Kimura, T. Suzuki, and Y. Itayama: *Trans. Jpn. Inst. Met.*, **14**, 135 (1973).
23) A. J. Perry: *J. Less-Common Met.*, **51**, 153 (1977).

Received Feb. 23, 2015; Revised Mar. 31, 2016; Accepted May 26, 2016

J. Magn. Soc. Jpn., **40**, 137-147 (2016)

<Paper>

Influence of Composition on the Crystal Structure of Fe-Ni Alloy Epitaxial Thin Film Deposited on Cr(211) Underlayer

Shigeyuki Minakawa[1], Mitsuru Ohtake[1], Masaaki Futamoto[1], Fumiyoshi Kirino[2], and Nobuyuki Inaba[3]

[1]Faculty of Science and Engineering, Chuo University, *1-13-27 Kasuga, Bunkyo-ku, Tokyo 112-8551, Japan*
[2]Graduate School of Fine Arts, Tokyo University of the Arts, *12-8 Ueno-koen, Taito-ku, Tokyo 110-8714, Japan*
[3]Faculty of Engineering, Yamagata University, *4-3-16 Jyonan, Yonezawa, Yamagata 992-8510, Japan*

$Fe_{100-x}Ni_x$ (x = 0–100 at. %) alloy epitaxial films of 10 nm thickness are prepared on Cr(211) underlayers at room temperature by using a radio-frequency magnetron sputtering system. The film growth behavior and the crystallographic properties are investigated by *in-situ* reflection high-energy electron diffraction and pole-figure X-ray diffraction. bcc(211) crystal epitaxially nucleates on the underlayer for the $Fe_{100-x}Ni_x$ films with x = 0–70 at. %. The bcc structure is stabilized up to 10 nm thickness for the compositional range of x = 0–50 at. %, whereas the $Fe_{40}Ni_{60}$ and the $Fe_{30}Ni_{70}$ crystals with bcc structure (x = 60–70 at. %) start to transform into fcc structure with increasing the thickness beyond 2 and 5 nm, respectively. The bcc-fcc phase transformation occurs through atomic displacements parallel to bcc(110) and bcc(101) close-packed planes which are 60° canted from the perpendicular direction. The crystallographic orientation relationship is similar to the Kurdjumov-Sachs relationship. When the x value is increased beyond 80 at. %, metastable hcp($1\bar{1}00$) crystal coexists with bcc(211) crystal. The volume ratio of hcp to bcc crystal increases as the x value increases from 80 to 100 at. %. With increasing the thickness, the hcp crystal also starts to transform into fcc structure through atomic displacement parallel to hcp(0001) close-packed plane, which is similar to the case of bulk phase transformation in the Shoji-Nishiyama relationship.

Key words: Fe-Ni alloy thin film, epitaxial growth, bcc, fcc, hcp, crystal structure, phase transformation

1. Introduction

Thin films of 3*d* ferromagnetic transition metals or their alloys have been widely studied for applications such as magnetic sensors, magnetic recording media, etc. Recently, magnetic films with metastable structures have attracted much attention, since new possibilities are recognized. For example, magnetic tunnel junction elements prepared by employing Co films with metastable bcc structure have been reported to show high tunnel magnetoresistance ratios[1–3]. The magnetic and electronic properties are greatly affected by their crystal structures. It is thus important to understand the formation conditions of films with metastable structures.

Fe, Ni, and Fe-Ni alloy materials are typical soft magnetic materials. In the bulk Fe-Ni binary alloy system[4], there are bcc (*A*2) and fcc (*A*1, $L1_2$) phases. On the contrary, metastable hcp (*A*3) phase has been recognized for Ni and $Fe_{20}Ni_{80}$ (at. %) films epitaxially grown on Cr[5–9], V[9], Au[10,11], MgO[12,13], and Ru[14] materials. Epitaxial thin film growth technique has a possibility in forming films with metastable structures. In our previous studies[6–8], Ni and $Fe_{20}Ni_{80}$ films of 40 nm thickness were sputter-deposited on Cr(211) underlayers at room temperature (RT). The crystallographic property during film formation was investigated by *in-situ* reflection high-energy electron diffraction (RHEED). hcp-Ni and hcp-$Fe_{20}Ni_{80}$ crystals of ($1\bar{1}00$) orientation nucleated on the underlayers. However with increasing the thickness, the hcp crystal started to transform into fcc structure and the volume ratio of hcp to transformed fcc crystal increased for both films.

The crystallographic properties are considered to be influenced by the film composition. However, the compositional dependence has not been made clear, yet. In the present study, $Fe_{100-x}Ni_x$ films are prepared on Cr(211) underlayers by varying the composition in the full range, x = 0–100 at. %. The growth behavior and the detailed structure property are investigated by *in-situ* RHEED and pole-figure X-ray diffraction (XRD).

2. Experimental Procedure

Thin films were deposited on polished MgO(110) single-crystal substrates by using a radio-frequency (RF) magnetron sputtering system with the base pressure lower than 4×10^{-7} Pa. Fe, Ni, and Cr targets of 3 inch diameter were used and the respective RF powers were fixed at 50, 58, and 40 W. The distance between target and substrate and the Ar gas pressure were kept constant at 150 mm and 0.67 Pa, respectively. Under the conditions, the deposition rate was 0.02 nm/s for all the materials.

MgO substrates were heated at 600 °C for 1 hour before film formation to obtain clean surfaces. 10-nm-thick Cr underlayers were deposited on the substrates at 300 °C. The substrate temperature was used to promote epitaxial growth of Cr underlayer on

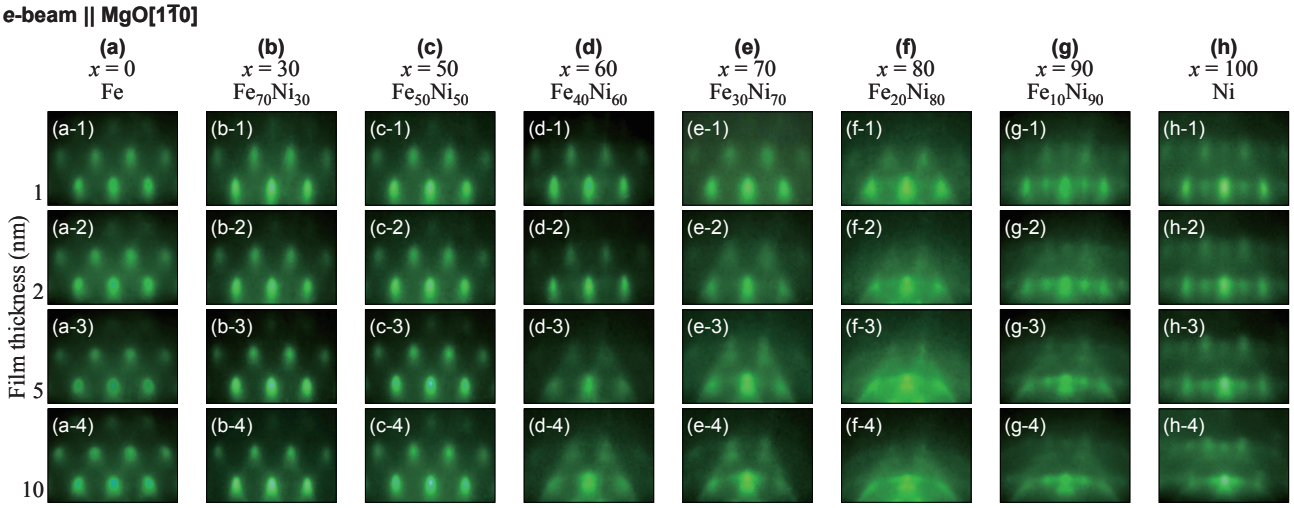

Fig. 1 RHEED patterns observed during formation of (a) Fe, (b) $Fe_{70}Ni_{30}$, (c) $Fe_{50}Ni_{50}$, (d) $Fe_{40}Ni_{60}$, (e) $Fe_{30}Ni_{70}$, (f) $Fe_{20}Ni_{80}$, (g) $Fe_{10}Ni_{90}$, and (h) Ni films on Cr(211) underlayers. The film thicknesses are (a-1)–(h-1) 1 nm, (a-2)–(h-2) 2 nm, (a-3)–(h-3) 5 nm, and (a-4)–(h-4) 10 nm. The incident electron beam is parallel to MgO[1$\bar{1}$0].

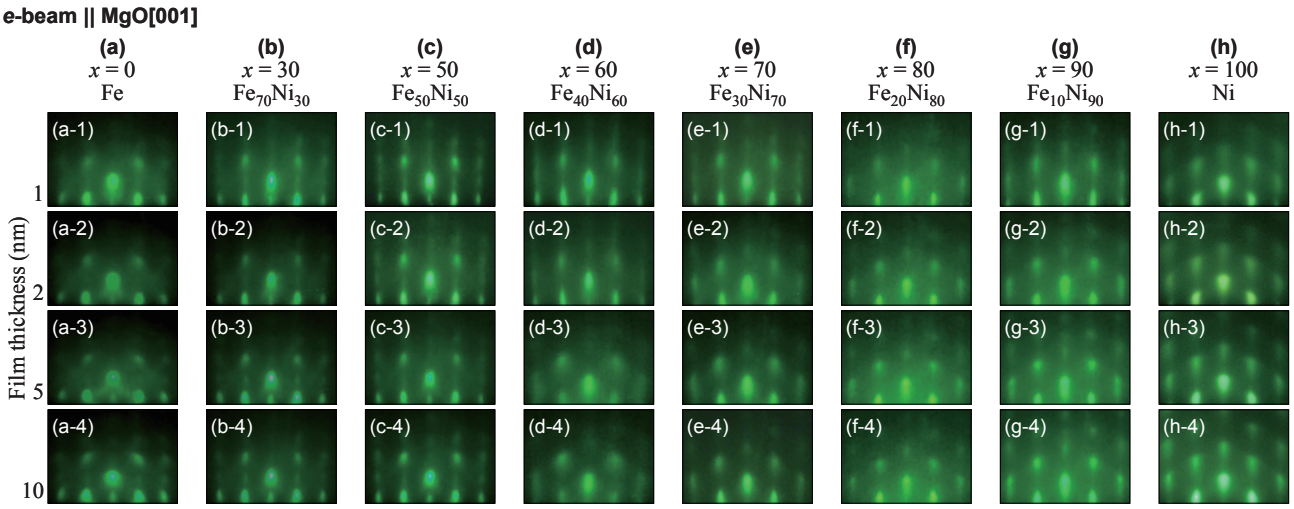

Fig. 2 RHEED patterns observed during formation of (a) Fe, (b) $Fe_{70}Ni_{30}$, (c) $Fe_{50}Ni_{50}$, (d) $Fe_{40}Ni_{60}$, (e) $Fe_{30}Ni_{70}$, (f) $Fe_{20}Ni_{80}$, (g) $Fe_{10}Ni_{90}$, and (h) Ni films on Cr(211) underlayers. The film thicknesses are (a-1)–(h-1) 1 nn, (a-2)–(h-2) 2 nm, (a-3)–(h-3) 5 nm, and (a-4)–(h-4) 10 nm. The incident electron beam is parallel to MgO[001].

MgO(110) substrate. The crystallographic orientation relationship between Cr underlayer and MgO substrate was Cr(211)[1$\bar{1}\bar{1}$], [$\bar{1}$11] || MgO(110)[1$\bar{1}$0].[6] After cooling the samples down to RT, $Fe_{100-x}Ni_x$ (x = 0, 30, 50, 60, 70, 80, 90, 100 at. %) alloy films of 10 nm thickness were formed on the Cr underlayers by alternative deposition of Fe and Ni layers. The layer structure was [Fe(1 – δ nm)/Ni(δ nm)]$_{10}$/Cr(10 nm)/MgO. The alloy formation and the film uniformity were checked by X-ray reflection. The Ni-Fe alloy composition was controlled by changing the δ value ($0 \leq \delta \leq 1$). The film composition was confirmed by energy dispersive X-ray spectroscopy and the errors were less than 3 at. % from the x values.

The film surface structure during growth process was observed by RHEED. The resulting film structure was investigated by $2\theta/\omega$-scan out-of-plane and pole-figure XRDs with Cu-Kα radiation (λ = 0.15418 nm). The surface morphology was observed by atomic force microscopy (AFM). The magnetization curves were measured by vibrating sample magnetometry.

3. Results and Discussion

3.1 Structure of $Fe_{100-x}Ni_x$ films ($0 \leq x \leq 50$ at. %)

Figures 1(a)–(c) and 2(a)–(c) show the RHEED patterns observed during formation of $Fe_{100-x}Ni_x$ films with x = 0–50 at. % on the Cr(211) underlayers. Here, two kinds of incident electron beam direction are used to identify the variant structure. The electron beam is parallel to MgO[1$\bar{1}$0] in Figs. 1(a)–(c), whereas that is parallel to MgO[001] in Figs. 2(a)–(c). MgO[001] is the

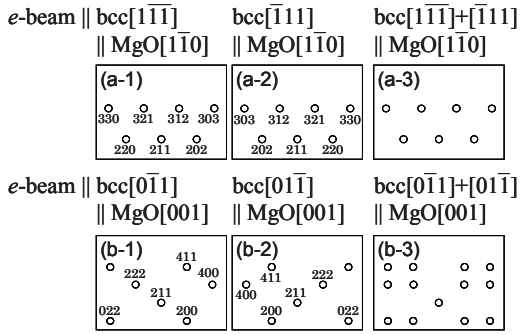

Fig. 3 Schematic diagrams of RHEED patterns simulated for bcc(211) crystal. The incident electron beam is parallel to (a-1) bcc[1$\bar{1}\bar{1}$], (a-2) bcc[$\bar{1}$11], (b-1) bcc[0$\bar{1}$1], or (b-2) bcc[01$\bar{1}$]. Schematic diagrams of (a-3) and (b-3) are drawn by overlapping (a-1) and (a-2) and by overlapping (b-1) and (b-2), respectively.

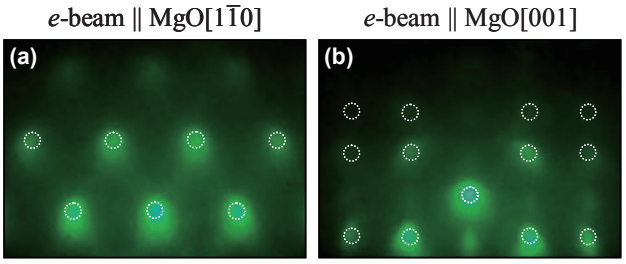

Fig. 4 RHEED patterns observed for a 10-nm-thick Fe film deposited on Cr(211) underlayer hetero-epitaxially grown on MgO(110) substrate [Figs. 1(a-4), 2(a-4)] overlapped with the reflection spots simulated for bcc(211) bi-crystal [Figs. 3(a-3), (b-3)]. The incident electron beam is parallel to (a) bcc[1$\bar{1}\bar{1}$]+bcc[$\bar{1}$11] || MgO[1$\bar{1}$0] or (b) bcc[0$\bar{1}$1]+bcc[01$\bar{1}$] || MgO[001].

direction rotated around the film normal by 90° with respect to MgO[1 $\bar{1}$ 0]. Clear RHEED patterns are observed from the beginnings till the ends of film formation. The films are epitaxially growing on the underlayers for the compositional range.

Possible diffraction patterns were calculated for bcc (*A*2) crystal. Figures 3(a-1)–(b-2) show the schematic diagrams of diffraction patterns of bcc(211) crystal simulated by making the incident electron beam parallel to bcc[1$\bar{1}\bar{1}$], bcc[$\bar{1}$11], bcc[0$\bar{1}$1], or bcc[01$\bar{1}$]. bcc[1$\bar{1}\bar{1}$] or bcc[$\bar{1}$11] is the direction rotated around the film normal by 90° with respect to bcc[0$\bar{1}$1] or bcc[01$\bar{1}$]. The experimental RHEED data shown in Figs. 1(a)–(c) (*e*-beam || MgO[1$\bar{1}$0]) are in agreement with both simulation results shown in Fig. 3(a-1) (*e*-beam || bcc[1$\bar{1}\bar{1}$]) and Fig. 3(a-2) (*e*-beam || bcc[$\bar{1}$11]). However, the observed RHEED patterns shown in Figs. 2(a)–(c) (*e*-beam || MgO[001]) are partially matching with the calculated patterns of Fig. 3(b-1) (*e*-beam || bcc[0$\bar{1}$1]) and Fig. 3(b-2) (*e*-beam || bcc[01$\bar{1}$]). Therefore, there is a possibility that bcc(211) bi-crystal is formed on the underlayer. Figures 3(a-3) and (b-3) are the schematic diagrams obtained by overlapping Figs. 3(a-1) and (a-2) and by overlapping Figs. 3(b-1) and (b-2), respectively.

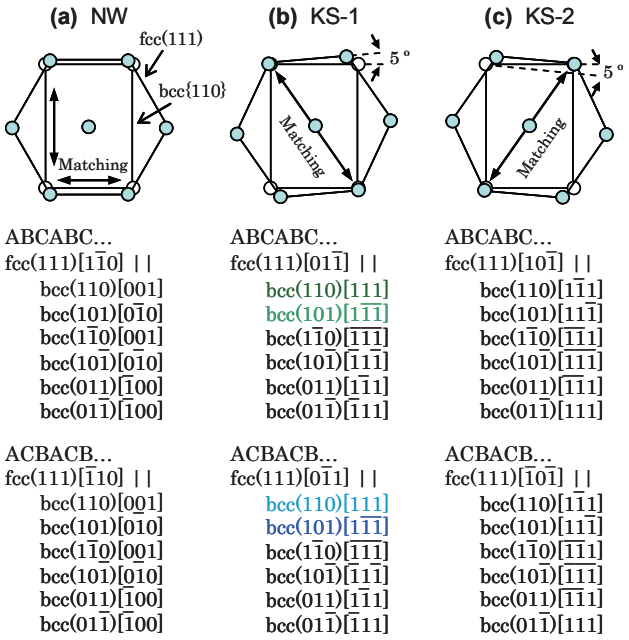

Fig. 5 Schematic diagrams and crystallographic orientation relationships of (a) NW, (b) KS-1, and (c) KS-2.

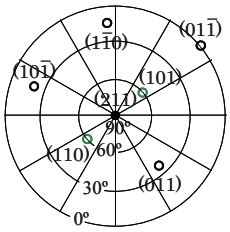

Fig. 6 Pole-figure map showing the configurations of bcc{110} planes around bcc(211) pole.

The observed RHEED patterns agree very well with the overlapped patterns of Figs. 3(a-3) and (b-3), as shown in Fig. 4. The crystallographic orientation relationships between bcc(211) crystal and MgO(110) substrate are thus determined as follows,

bcc-$Fe_{100-x}Ni_x$(211)[1$\bar{1}\bar{1}$] || Cr(211)[1$\bar{1}\bar{1}$], [$\bar{1}$11]
|| MgO(110)[1$\bar{1}$0], (Type I)

bcc-$Fe_{100-x}Ni_x$(211)[$\bar{1}$11] || Cr(211)[1$\bar{1}\bar{1}$], [$\bar{1}$11]
|| MgO(110)[1$\bar{1}$0]. (Type II)

The films consist of two bcc(211) variants whose orientations are rotated around the film normal by 180° each other.

3.2 Structure of $Fe_{100-x}Ni_x$ films ($60 \leq x \leq 70$ at. %)

Figures 1[(d), (e)] and 2[(d), (e)] show the RHEED patterns observed for $Fe_{40}Ni_{60}$ and $Fe_{30}Ni_{70}$ films. RHEED patterns corresponding to the simulated diffraction patterns from bcc(211) bi-crystal [Figs. 3(a-3), (b-3)] are observed for the $Fe_{40}Ni_{60}$ film thinner than 2

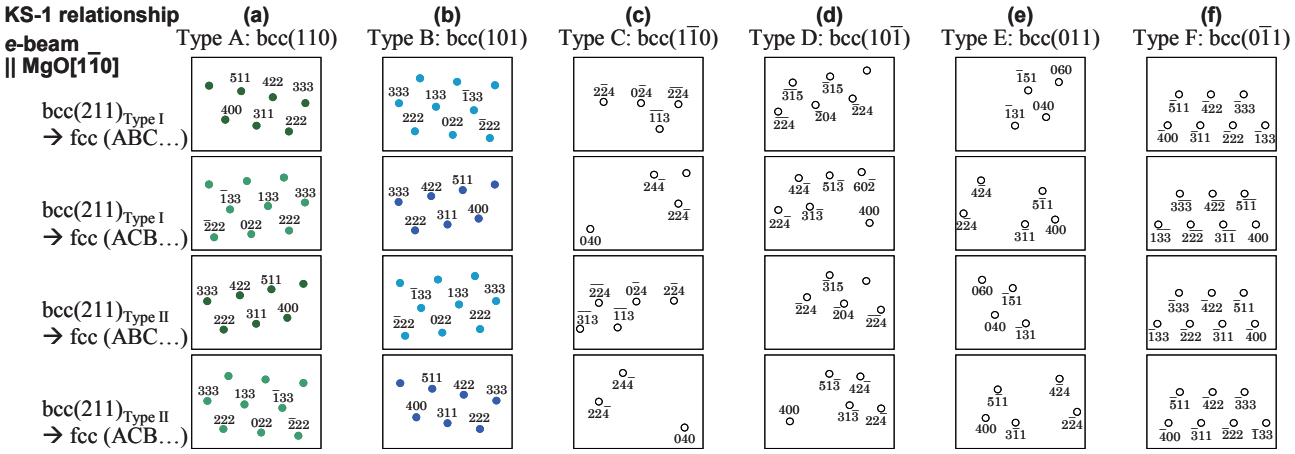

Fig. 7 Schematic diagrams of RHEED patterns simulated for fcc crystals with the atomic stacking sequences of ABCABC… and ACBACB… along fcc[111] transformed from bcc(211) crystals with I- and II-type epitaxial orientation relationships through atomic displacements parallel to (a) bcc(110), (b) bcc(101), (c) bcc(011), (d) bcc(10$\bar{1}$), (e) bcc(1$\bar{1}$0), and (f) bcc(0$\bar{1}$1) planes in the KS-1 relationship. The incident electron beam is parallel to MgO[1$\bar{1}$0].

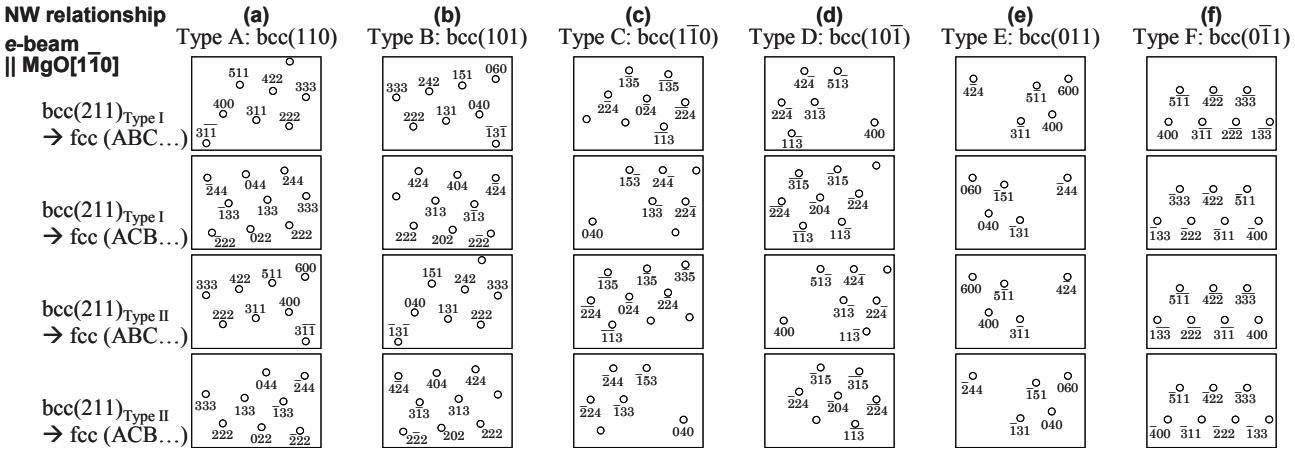

Fig. 8 Schematic diagrams of RHEED patterns simulated for fcc crystals with the atomic stacking sequences of ABCABC… and ACBACB… along fcc[111] transformed from bcc(211) crystals with I- and II-type epitaxial orientation relationships through atomic displacements parallel to (a) bcc(110), (b) bcc(101), (c) bcc(011), (d) bcc(10$\bar{1}$), (e) bcc(1$\bar{1}$0), and (f) bcc(0$\bar{1}$1) planes in the NW relationship. The incident electron beam is parallel to MgO[1$\bar{1}$0].

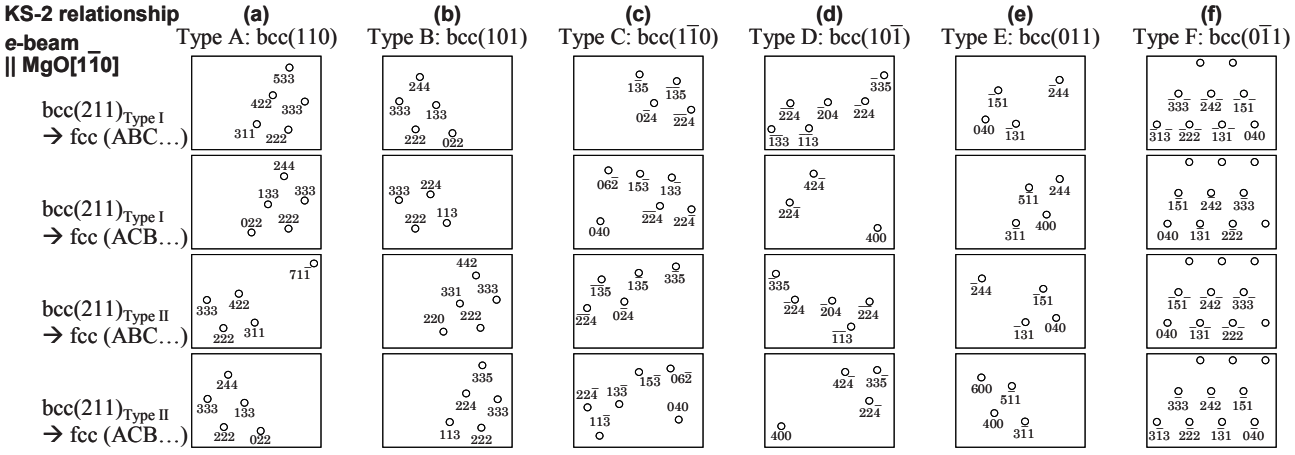

Fig. 9 Schematic diagrams of RHEED patterns simulated for fcc crystals with the atomic stacking sequences of ABCABC… and ACBACB… along fcc[111] transformed from bcc(211) crystals with I- and II-type epitaxial orientation relationships through atomic displacements parallel to (a) bcc(110), (b) bcc(101), (c) bcc(011), (d) bcc(10$\bar{1}$), (e) bcc(1$\bar{1}$0), and (f) bcc(0$\bar{1}$1) planes in the KS-2 relationship. The incident electron beam is parallel to MgO[1$\bar{1}$0].

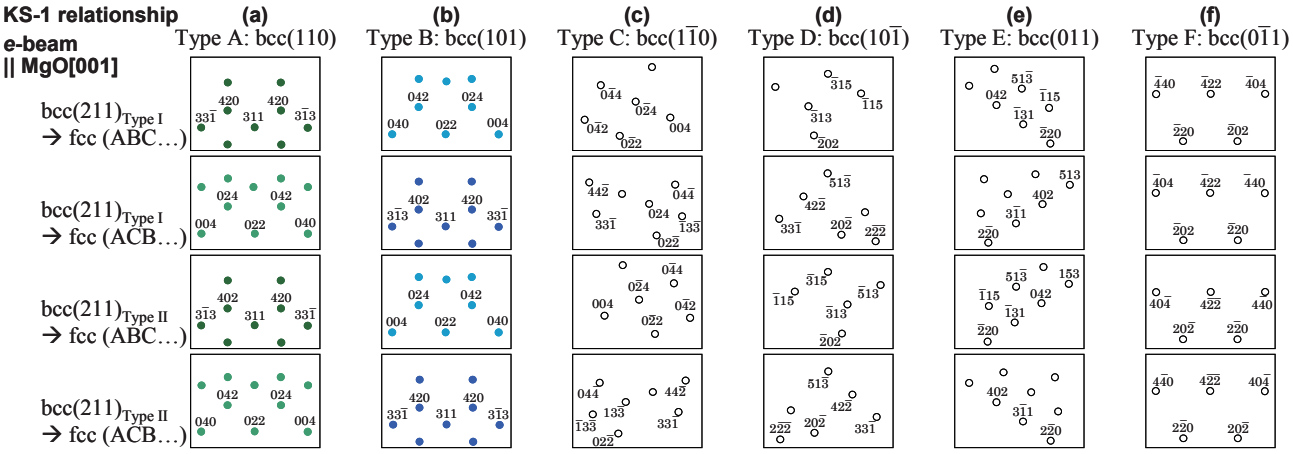

Fig. 10 Schematic diagrams of RHEED patterns simulated for fcc crystals with the atomic stacking sequences of ABCABC… and ACBACB… along fcc[111] transformed from bcc(211) crystals with I- and II-type epitaxial orientation relationships through atomic displacements parallel to (a) bcc(110), (b) bcc(101), (c) bcc(011), (d) bcc(10$\bar{1}$), (e) bcc(1$\bar{1}$0), and (f) bcc(0$\bar{1}$1) planes in the KS-1 relationship. The incident electron beam is parallel to MgO[001].

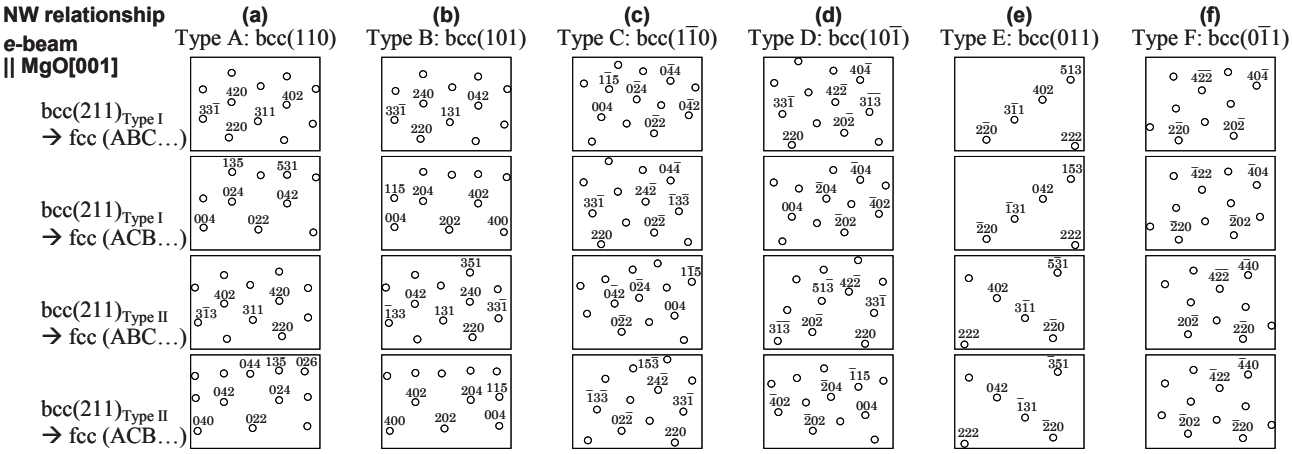

Fig. 11 Schematic diagrams of RHEED patterns simulated for fcc crystals with the atomic stacking sequences of ABCABC… and ACBACB… along fcc[111] transformed from bcc(211) crystals with I- and II-type epitaxial orientation relationships through atomic displacements parallel to (a) bcc(110), (b) bcc(101), (c) bcc(011), (d) bcc(10$\bar{1}$), (e) bcc(1$\bar{1}$0), and (f) bcc(0$\bar{1}$1) planes in the NW relationship. The incident electron beam is parallel to MgO[001].

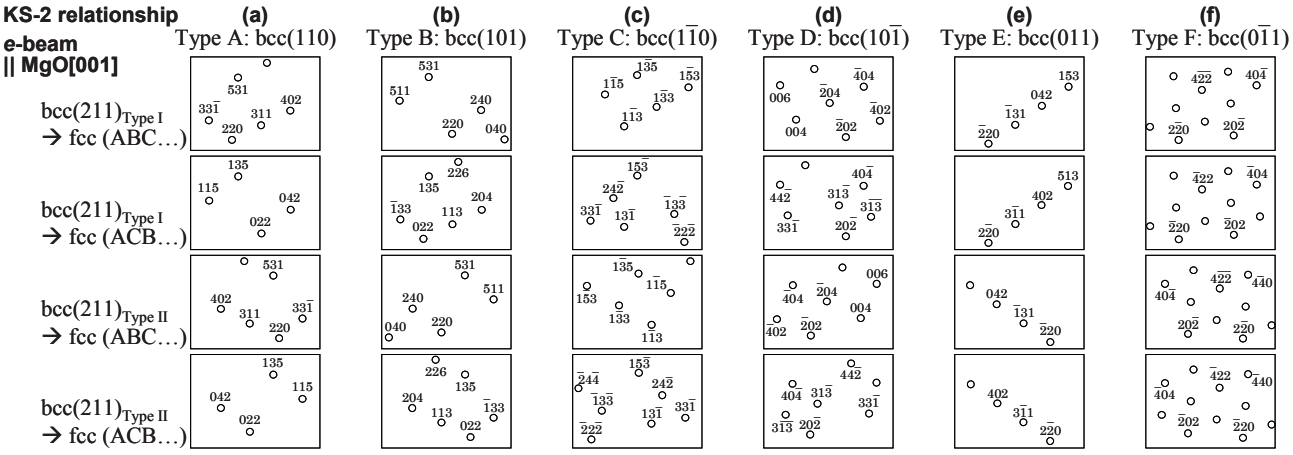

Fig. 12 Schematic diagrams of RHEED patterns simulated for fcc crystals with the atomic stacking sequences of ABCABC… and ACBACB… along fcc[111] transformed from bcc(211) crystals with I- and II-type epitaxial orientation relationships through atomic displacements parallel to (a) bcc(110), (b) bcc(101), (c) bcc(011), (d) bcc(10$\bar{1}$), (e) bcc(1$\bar{1}$0), and (f) bcc(0$\bar{1}$1) planes in the KS-2 relationship. The incident electron beam is parallel to MgO[001].

nm [Figs. 1(d-1)–(d-2), 2(d-1)–(d-2)] and the $Fe_{30}Ni_{70}$ film thinner than 1 nm [Figs. 1(e-1), 2(e-1)]. With further increasing the thickness [Figs. 1(d-3)–(d-4), 1(e-2)–(e-4), 2(d-3)–(d-4), 2(e-2)–(e-4)], RHEED spots become broader and diffraction spots other than bcc crystal appear for both films, indicating that phase transformation is taking place. The thickness stability of bcc crystal formation is decreased as the x value increases from 50 to 70 at. %.

When a bulk bcc material transforms into fcc structure, there are two possible crystallographic orientation relationships of Nishiyama-Wasserman[15,16] (NW) and Kurdjumov-Sachs[17] (KS),

$$\begin{aligned}&\mathrm{fcc}(111)[1\bar{1}0]_{\mathrm{ABCABC\ldots}},\ \mathrm{fcc}(111)[\bar{1}10]_{\mathrm{ACBACB\ldots}}\\ &\quad\parallel\ \mathrm{bcc}(110)[001],\ \mathrm{bcc}(101)[0\bar{1}0],\ \mathrm{bcc}(1\bar{1}0)[001],\\ &\qquad\mathrm{bcc}(10\bar{1})[0\bar{1}0],\ \mathrm{bcc}(011)[\bar{1}00],\ \mathrm{bcc}(01\bar{1})[\bar{1}00],\quad(\mathrm{NW})\end{aligned}$$

$$\begin{aligned}&\mathrm{fcc}(111)[01\bar{1}]_{\mathrm{ABCABC\ldots}},\ \mathrm{fcc}(111)[0\bar{1}1]_{\mathrm{ACBACB\ldots}}\\ &\quad\parallel\ \mathrm{bcc}(110)[111],\ \mathrm{bcc}(101)[1\bar{1}1],\ \mathrm{bcc}(1\bar{1}0)[\bar{1}11],\\ &\qquad\mathrm{bcc}(10\bar{1})[\bar{1}11],\ \mathrm{bcc}(011)[1\bar{1}1],\ \mathrm{bcc}(01\bar{1})[\bar{1}11],\quad(\mathrm{KS\text{-}1})\end{aligned}$$

$$\begin{aligned}&\mathrm{fcc}(111)[10\bar{1}]_{\mathrm{ABCABC\ldots}},\ \mathrm{fcc}(111)[\bar{1}01]_{\mathrm{ACBACB\ldots}}\\ &\quad\parallel\ \mathrm{bcc}(110)[111],\ \mathrm{bcc}(101)[1\bar{1}1],\ \mathrm{bcc}(1\bar{1}0)[\bar{1}11],\\ &\qquad\mathrm{bcc}(10\bar{1})[\bar{1}11],\ \mathrm{bcc}(011)[1\bar{1}1],\ \mathrm{bcc}(01\bar{1})[\bar{1}11].\quad(\mathrm{KS\text{-}2})\end{aligned}$$

The phase transformation occurs through atomic displacements from bcc(110), bcc(101), bcc(011), bcc(10$\bar{1}$), bcc(1$\bar{1}$0), and bcc(0$\bar{1}$1) close-packed planes to fcc(111) plane, as shown in Fig. 5. The configurations of bcc{110} planes in a bcc crystal with the (211) plane parallel to the substrate surface are shown in the pole-figure map of Fig. 6.

Figures 7–12 show the schematic diagrams of RHEED patterns simulated for fcc ($A1$) crystals with the atomic stacking sequences of ABCABC… and ACBACB… along fcc[111] transformed from bcc(211) crystals with I- and II-type orientation relationships through atomic displacements parallel to bcc{110} planes in the KS-1 [Figs. 7, 10], the NW [Figs. 8, 11], and the KS-2 [Figs. 9, 12] relationships. Figures 13(a)–(f) are drawn by overlapping all the schematic diagrams shown in Figs. 7–12, respectively. Here, the electron beam is parallel to MgO[1$\bar{1}$0] in Figs. 13(a)–(c), whereas that is parallel to MgO[001] in Figs. 13(d)–(f). The RHEED patterns observed for the $Fe_{40}Ni_{60}$ film thicker than 5 nm [Figs. 1(d-3)–(d-4), 2(d-3)–(d-4)] and the $Fe_{30}Ni_{70}$ film thicker than 2 nm [Figs. 1(e-2)–(e-4), 2(e-2)–(e-4)] are different from any patterns shown in Fig. 13. The bcc{110} slide planes where the phase transformation occurs are considered to be influenced by the strain caused by accommodation of the lattice misfit between film and underlayer[18].

Figures 14(a)–(f) are obtained by overlapping the schematic diagrams of patterns simulated for fcc crystals transformed through atomic displacements parallel to bcc(110) and bcc(101) planes [Figs. 7[(a), (b)], 8[(a), (b)], 9[(a), (b)], 10[(a), (b)], 11[(a), (b)], 12[(a), (b)]].

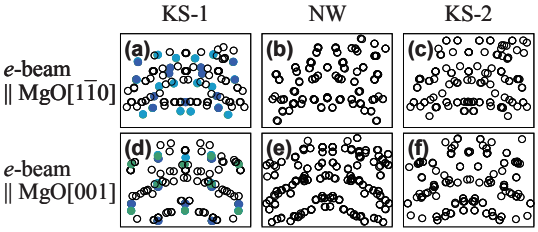

Fig. 13 Schematic diagrams of RHEED patterns simulated for fcc crystals transformed through atomic displacements from bcc(110), bcc(101), bcc(011), bcc(10$\bar{1}$), bcc(1$\bar{1}$0), and bcc(0$\bar{1}$1) planes to fcc(111) plane in [(a), (d)] the KS-1, [(b), (e)] the NW, and [(c), (f)] the KS-2 relationships. The incident electron beam is parallel to (a)–(c) MgO[1$\bar{1}$0] or (d)–(f) MgO[001]. The schematic diagrams of (a)–(f) are drawn by overlapping all the schematic diagrams shown in Figs. 7–12, respectively.

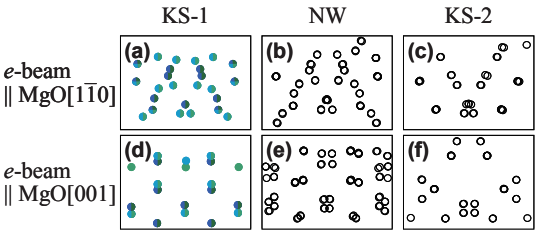

Fig. 14 Schematic diagrams of RHEED patterns simulated for fcc crystals transformed through atomic displacements from bcc(110) and bcc(101) planes to fcc(111) plane in [(a), (d)] the KS-1, [(b), (e)] the NW, and [(c), (f)] the KS-2 relationships. The incident electron beam is parallel to (a)–(c) MgO[1$\bar{1}$0] or (d)–(f) MgO[001]. The schematic diagrams of (a)–(f) are drawn by overlapping all the schematic diagrams shown in Figs. 7[(a), (b)]–12[(a), (b)], respectively.

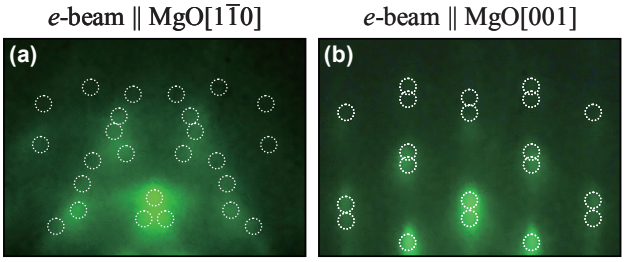

Fig. 15 RHEED patterns observed for a 10-nm-thick $Fe_{30}Ni_{70}$ film deposited on Cr(211) underlayer hetero-epitaxially grown on MgO(110) substrate [Figs. 1(e-4), 2(e-4)] overlapped with the reflection spots simulated for fcc crystals transformed through atomic displacements from bcc(110) and bcc(101) planes to fcc(111) plane in the KS-1 relationship [Figs. 14(a), (d)]. The incident electron beam is parallel to (a) MgO[1$\bar{1}$0] or (b) MgO[001].

The RHEED patterns observed for the $Fe_{40}Ni_{60}$ film thicker than 5 nm [Figs. 1(d-3)–(d-4), 2(d-3)–(d-4)] and the $Fe_{30}Ni_{70}$ film thicker than 2 nm [Figs. 1(e-2)–(e-4), 2(e-2)–(e-4)] are in agreement with the simulated patterns of Figs. 14(a) and (d), as shown in Fig. 15. The

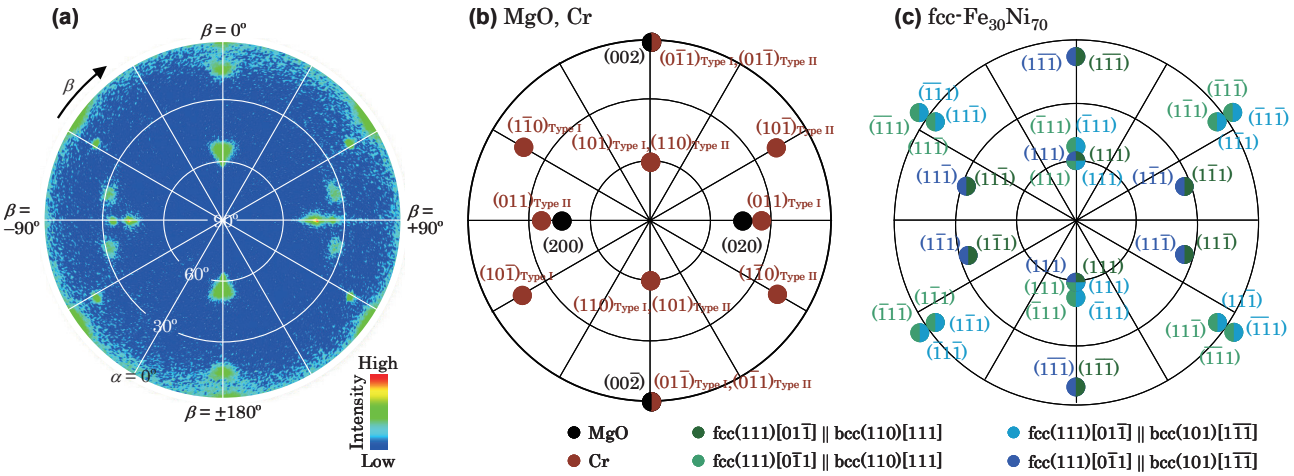

Fig. 16 (a) Pole-figure XRD pattern measured for a 40-nm-thick $Fe_{30}Ni_{70}$ film deposited on Cr(211) underlayer hetero-epitaxially grown on MgO(110) substrate. The diffraction angle of $2\theta B$ is fixed at 44°. The intensity is shown in logarithmic scale. [(b), (c)] Schematic diagrams obtained (b) by overlapping the diffraction patterns simulated for MgO(110) substrate and Cr(211) underlayer and (c) by overlapping the patterns calculated for the fcc crystals transformed from bcc structure in the crystallographic orientation relationships determined by RHEED.

result shows that the phase transformation is not taking place through atomic displacements from six bcc{110} planes but from bcc(110) and bcc(101) planes, which are 60° inclined from the perpendicular direction, in the KS-1 relationship.

When the bcc(211) epitaxial bicrystalline films transform into fcc structure through atomic displacements parallel to bcc(110) and bcc(101) planes in the KS relationship, the films consist of four fcc crystals. fcc(311) is 0.5° tilted from the substrate surface for the fcc crystals with the staking sequences of ABCABC… and ACBACB… along fcc[111] transformed from bcc(211) crystals with I- and II-type relationships through atomic displacements parallel to bcc(110) and bcc(101) planes, respectively. On the other hand, fcc(011) plane is 5° canted from the substrate surface for the fcc crystals with the staking sequences of ACBACB… and ABCABC… along fcc[111] transformed from bcc(211) crystals with I- and II-type relationships through atomic displacements parallel to bcc(110) and bcc(101) planes, respectively. These low-index planes of transformed fcc crystals tend to be more inclined from the substrate surface in the cases of NW and KS-2 relationships. Therefore, the phase transformation in the KS-1 relationship seems to be favored.

In order to confirm the phase transformation orientation relationships, pole-figure XRD was carried out. Figure 16(a) shows the pole-figure XRD pattern of a 40-nm-thick $Fe_{30}Ni_{70}$ film deposited on Cr(211) underlayer hetero-epitaxially grown on MgO(110) substrate. Here, the film thickness of 40 nm is employed so that the reflections from transformed fcc crystals are detected more strongly. The diffraction angle of $2\theta B$ is fixed at 44°, where MgO{200}, Cr{110}, and fcc-$Fe_{30}Ni_{70}${111} reflections are expected to be detectable. Figures 16(b) and (c), respectively, show the schematic diagrams obtained by overlapping the diffraction patterns simulated for MgO(110) substrate and Cr(211) underlayer and by overlapping the patterns calculated for the fcc crystals transformed from bcc structure in the crystallographic orientation relationships determined by RHEED. The measured pole-figure XRD pattern of Fig. 16(a) apparently agrees with an overlap of the simulated patterns of Figs. 16(b) and (c). The pole-figure XRD confirms the orientation relationships determined by RHEED.

3.3 Structure of $Fe_{100-x}Ni_x$ films ($80 \leq x \leq 100$ at. %)

Figures 1[(g), (h)] and 2[(g), (h)] show the RHEED patterns observed for $Fe_{10}Ni_{90}$ and Ni films. Diffraction patterns from hcp(1$\bar{1}$00) surface shown in the schematic diagrams of Fig. 17 are overlapped with those from bcc(211) surface [Figs. 3(a-3), (b-3)] for the $Fe_{10}Ni_{90}$ film thinner than 1 nm [Figs. 1(g-1), 2(g-1)] and the Ni film thinner than 5 nm [Figs. 1(h-1)–(h-3), 2(h-1)–(h-3)], as shown in Fig. 18. Therefore, these films are composed of a mixture of hcp(1$\bar{1}$00) and bcc(211) crystals. $Fe_{10}Ni_{90}$ and Ni crystals with metastable hcp structure are stabilized through hetero-epitaxial growth on Cr(211) underlayer, similar to the cases of previous studies[5–8]. The crystallographic orientation relationship between hcp-$Fe_{100-x}Ni_x$(1$\bar{1}$00) crystal and Cr underlayer is

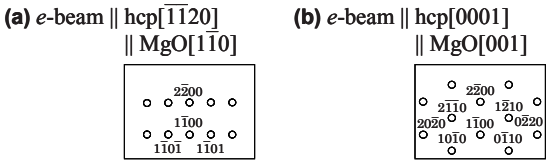

Fig. 17 Schematic diagrams of RHEED patterns simulated for hcp(1$\bar{1}$00) crystal. The incident electron beam is parallel to (a) hcp[11̄20] or (b) hcp[0001].

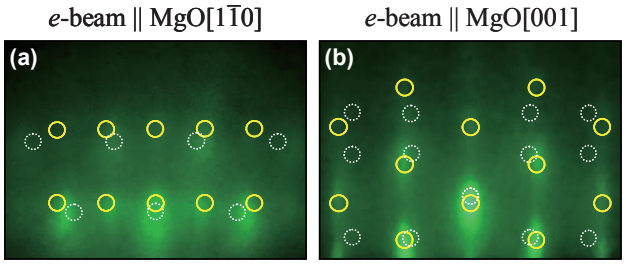

Fig. 18 RHEED patterns observed for a 1-nm-thick $Fe_{10}Ni_{90}$ film deposited on Cr(211) underlayer hetero-epitaxially grown on MgO(110) substrate [Figs. 1(g-1), 2(g-1)] overlapped with the reflection spots simulated for hcp(1$\bar{1}$00) [Fig. 17] and bcc(211) [Figs. 3(a-3), (b-3)] crystals. The incident electron beam is parallel to (a) MgO[1$\bar{1}$0] or (b) MgO[001]. The diffraction patterns consisting of yellow solid and white dotted circles correspond to Fig. 17 and Figs. 3[(a-3), (b-3)], respectively.

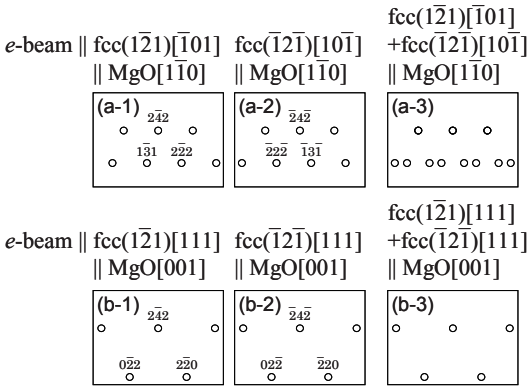

Fig. 19 Schematic diagrams of RHEED patterns simulated for fcc crystals with the atomic stacking sequences of [(a-1), (b-1)] ABCABC… and [(a-2), (b-2)] ACBACB… along fcc[111] transformed from hcp(1$\bar{1}$00) crystal with III-type orientation relationship through atomic displacement parallel to hcp(0001) plane in the SN relationship. The incident electron beam is parallel to (a) MgO[1$\bar{1}$0] or (b) MgO[001]. Schematic diagrams of (a-3) and (b-3) are drawn by overlapping (a-1) and (a-2) and by overlapping (b-1) and (b-2), respectively.

determined by RHEED as

hcp-$Fe_{100-x}Ni_x$(1$\bar{1}$00)[$\bar{1}\bar{1}$20] || Cr(211)[1$\bar{1}\bar{1}$], [$\bar{1}$11]
|| MgO(110)[1$\bar{1}$0]. (Type III)

As the thickness further increases [Figs. 1(g-2)–(g-4), 1(h-4), 2(g-2)–(g-4), 2(h-4)], RHEED spots become broader, suggesting that the phase transformations from hcp and bcc crystals to fcc structure are taking place. The details of hcp-fcc phase transformation in hcp(1$\bar{1}$00) film are shown in our previous paper[6]. The hcp-fcc transformation occurred through atomic displacement from hcp(0001) to fcc(111) plane. The crystallographic orientation relationship between hcp and fcc crystals was

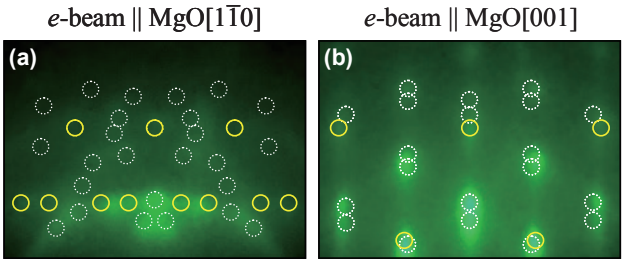

Fig. 20 RHEED patterns observed for a 10-nm-thick $Fe_{10}Ni_{90}$ film deposited on Cr(211) underlayer hetero-epitaxially grown on MgO(110) substrate [Figs. 1(g-4), 2(g-4)] overlapped with the reflection spots calculated for fcc crystals transformed through atomic displacements from hcp(0001) to fcc(111) plane in the SN relationship [Figs. 19(a-3), (b-3)] and the reflection spots simulated for fcc crystals transformed through atomic displacements from bcc(110) and bcc(101) planes to fcc(111) plane in the KS-1 relationship [Figs. 14(a), (d)]. The incident electron beam is parallel to (a) MgO[1$\bar{1}$0] or (b) MgO[001]. The diffraction patterns consisting of yellow solid and white dotted circles correspond to Fig. 19[(a-3), (b-3)]] and Figs. 14[(a-3), (b-3)], respectively.

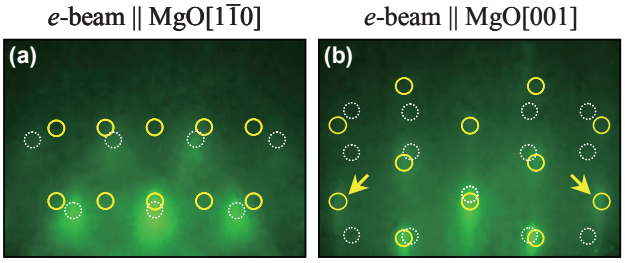

Fig. 21 RHEED patterns observed for a 1-nm-thick $Fe_{20}Ni_{80}$ film deposited on Cr(211) underlayer hetero-epitaxially grown on MgO(110) substrate [Figs. 1(f-1), 2(f-1)] overlapped with the reflection spots simulated for hcp(1$\bar{1}$00) [Fig. 17] and bcc(211) [Figs. 3(a-3), (b-3)] crystals. The incident electron beam is parallel to (a) MgO[1$\bar{1}$0] or (b) MgO[001]. The diffraction patterns consisting of yellow solid and white dotted circles correspond to Fig. 17 and Figs. 3[(a-3), (b-3)], respectively.

fcc(1$\bar{2}$1)[$\bar{1}$01], fcc($\bar{1}$2$\bar{1}$)[10$\bar{1}$] || hcp(1$\bar{1}$00)[$\bar{1}\bar{1}$20]
|| Cr(211)[1$\bar{1}\bar{1}$], [$\bar{1}$11]
|| MgO(110)[1$\bar{1}$0], (SN)

which was similar to the Shoji-Nishiyama (SN) relationship[19,20].

Figure 19 shows the schematic diagrams of RHEED patterns calculated for fcc crystals transformed in the SN relationship. The RHEED patterns observed for the $Fe_{10}Ni_{90}$ film thicker than 2 nm [Figs. 1(g-2)–(g-4), 2(g-2)–(g-4)] and the Ni film of 10 nm thickness [Figs. 1(h-4), 2(h-4)] are considered to be consisting of the diffraction patterns of Figs. 14[(a), (d)] and 19[(a-3), (b-3)], as shown in Fig. 20.

Figures 1(f) and 2(f) show the RHEED patterns observed during $Fe_{20}Ni_{80}$ film formation. The RHEED

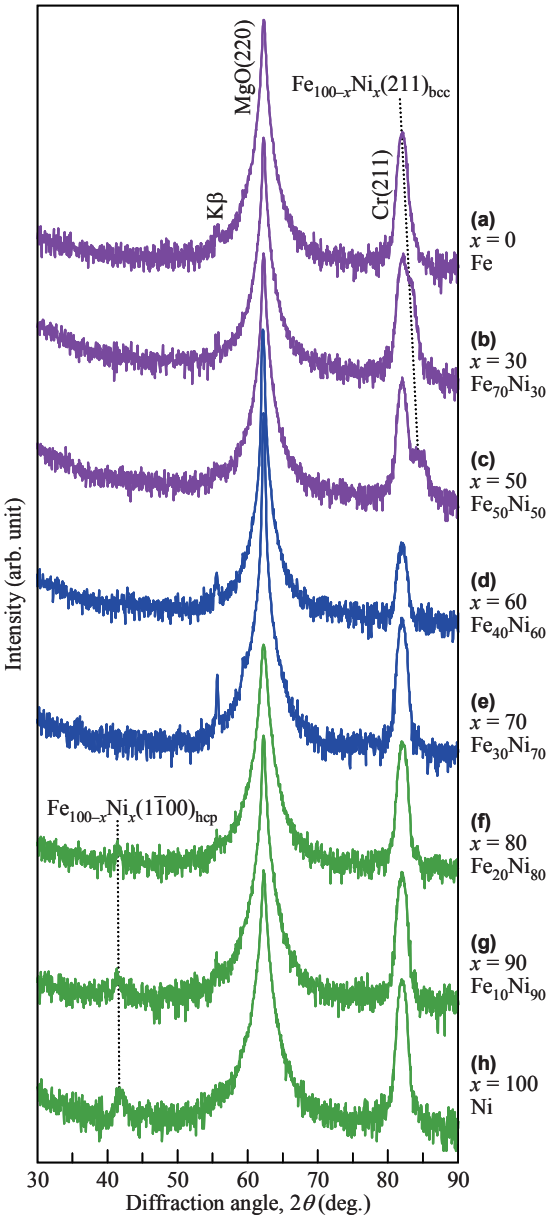

Fig. 22 Out-of-plane XRD patterns of (a) Fe, (b) $Fe_{70}Ni_{30}$, (c) $Fe_{50}Ni_{50}$, (d) $Fe_{40}Ni_{60}$, (e) $Fe_{30}Ni_{70}$, (f) $Fe_{20}Ni_{80}$, (g) $Fe_{10}Ni_{90}$, and (h) Ni films deposited on Cr(211) underlayers hetero-epitaxially grown on MgO(110) substrates. The intensity is shown in logarithmic scale.

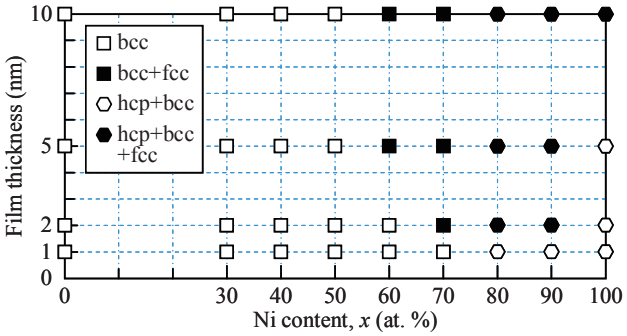

Fig. 23 Phase transformation map of $Fe_{100-x}Ni_x$ films.

patterns observed for the 1-nm-thick film [Figs. 1(f-1), 2(f-1)] seems to involve the reflection spots from hcp($1\bar{1}$ 00) crystal as shown in Fig. 21, though the reflection intensity of hcp($1\bar{1}00$) crystal is fairly weaker than that of bcc(211) crystal. With increasing the thickness beyond 2 nm [Figs. 1(f-2)–(f-4), 2(f-2)–(f-4)], the RHEED pattern changes to an overlap of diffraction patterns from fcc crystals transformed from bcc and hcp structures [Figs. 14[(a), (d)], 19[(a-3), (b-3)]].

Figure 22 shows the out-of-plane XRD patterns measured for the $Fe_{100-x}Ni_x$ films of 10 nm thickness with different compositions. bcc-$Fe_{100-x}Ni_x$(211) reflections are observed for the Fe, the $Fe_{70}Ni_{30}$, and the $Fe_{50}Ni_{50}$ films (x = 0–50 at. %), while those are absent for the $Fe_{40}Ni_{60}$ and the $Fe_{30}Ni_{70}$ films (x = 60–70 at. %) where the bcc-fcc phase transformation is taking place. hcp-$Fe_{100-x}Ni_x(1\bar{1}00)$ reflections are recognized not only for the $Fe_{10}Ni_{90}$ and the Ni films (x = 90–100 at. %) but also for the $Fe_{20}Ni_{80}$ film (x = 80 at. %). As the x value increases from 80 to 100 at. %, the intensity of hcp($1\ \bar{1}\ 00$) reflection increases, indicating that the volume of hcp crystal nucleated on Cr(211) underlayer is increased with increasing the Ni content. By considering the RHEED and the XRD data, the phase transformation map of $Fe_{100-x}Ni_x$ films is determined as shown in Fig. 23.

3.4 Surface morphology and magnetic property

Figure 24 shows the AFM images observed for the $Fe_{100-x}Ni_x$ films deposited on Cr(211) underlayers. These

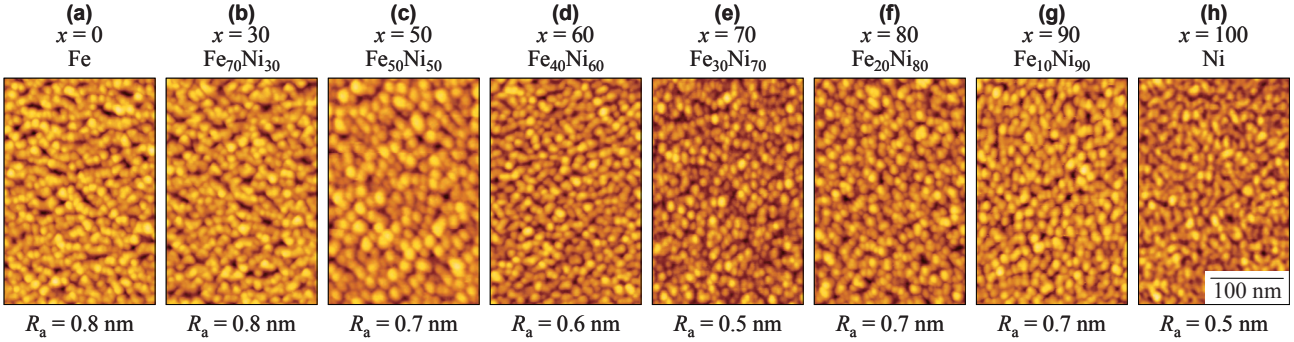

Fig. 24 AFM images observed for (a) Fe, (b) $Fe_{70}Ni_{30}$, (c) $Fe_{50}Ni_{50}$, (d) $Fe_{40}Ni_{60}$, (e) $Fe_{30}Ni_{70}$, (f) $Fe_{20}Ni_{80}$, (g) $Fe_{10}Ni_{90}$, and (h) Ni films deposited on Cr(211) underlayers hetero-epitaxially grown on MgO(110) substrates.

films have flat surfaces with the arithmetical mean roughness (R_a) values lower than 1 nm.

Figure 25 shows the magnetization curves measured for the $Fe_{100-x}Ni_x$ films. The magnetic field is applied along MgO[1$\bar{1}$0], MgO[001], or the direction rotated around the film normal by 51° with respect to MgO[1$\bar{1}$0], which is the direction obtained by inclining bcc[010] of bcc(211) crystals with I- and II-type orientation relationships to the film plane. The effective easy magnetization direction is observed along MgO[001] for the films with x = 0–70 at. %, whereas that is recognized along MgO[1$\bar{1}$0] for the films with x = 80–100 at. %. The magnetic properties seem to be delicately influenced by the crystal structure, the film composition, the configuration of transformed fcc crystals, etc.

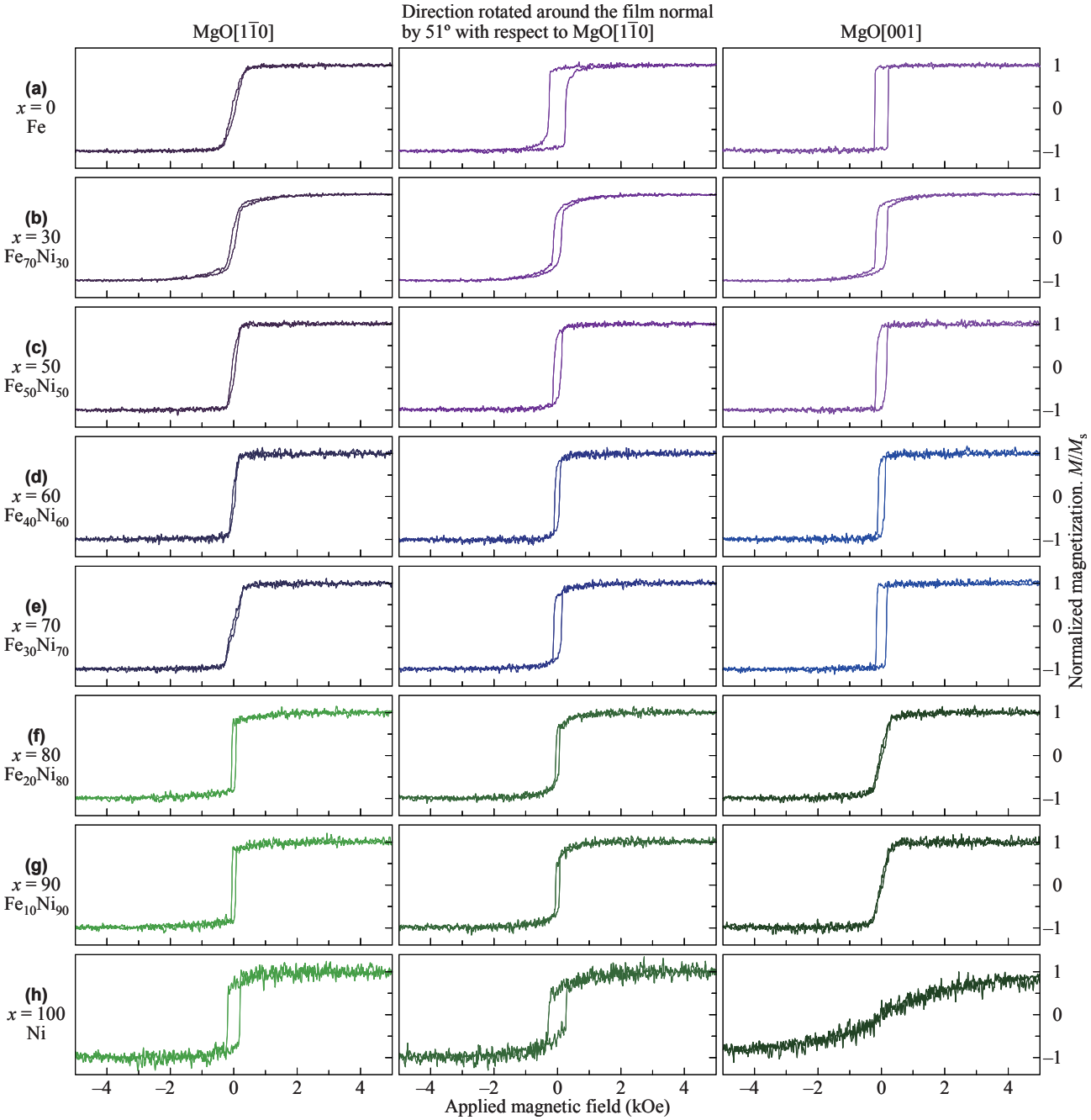

Fig. 25 Magnetization curves measured for (a) Fe, (b) $Fe_{70}Ni_{30}$, (c) $Fe_{50}Ni_{50}$, (d) $Fe_{40}Ni_{60}$, (e) $Fe_{30}Ni_{70}$, (f) $Fe_{20}Ni_{80}$, (g) $Fe_{10}Ni_{90}$, and (h) Ni films deposited on Cr(211) underlayers hetero-epitaxially grown on MgO(110) substrates. The magnetic field is applied along MgO[1$\bar{1}$0], MgO[001], or the direction rotated around the film normal by 51° with respect to MgO[1$\bar{1}$0], which is the direction obtained by inclining bcc[010] of bcc(211) crystals with I- and II-type orientation relationships to the film plane.

4. Conclusion

$Fe_{100-x}Ni_x$ alloy epitaxial films of 10 nm thickness are prepared on Cr(211) underlayers by varying the composition in the full range of x = 0–100 at. %. The film growth behavior and the crystallographic properties are investigated by RHEED and XRD. bcc(211) crystal nucleates on the underlayer for the $Fe_{100-x}Ni_x$ films with x = 0–70 at. %, whereas hcp($1\bar{1}00$) crystal coexists with bcc(211) crystal in the cases of x = 80–100 at. %. With increasing the thickness, the bcc(211) and/or the hcp($1\bar{1}00$) crystals start to transform into fcc structure for the films with $x \geq 60$ at. %. As the x value increases, the critical thickness up to which bcc crystal stability is maintained decreases, whereas that for hcp crystal increases. The bcc-fcc and the hcp-fcc phase transformations occur through atomic displacements from bcc(110) and bcc(101) close-packed planes and from hcp(0001) close-packed plane to fcc(111) close-packed plane, respectively. The crystallographic orientation relationships are similar to the Kurdjumov-Sachs and the Shoji-Nishiyama relationships.

Acknowledgments A part of this work was supported by JSPS KAKENHI Grant Numbers 25420294 and 26820117 and Chuo University Grant for Special Research.

References

1) X. -G. Zhang and W. H. Butler: *Phys. Rev. B*, **70**, 172407 (2004).
2) J. P. Velev, K. D. Belashchenko, D. A. Stewart, M. van Schifgaarde, S. S. Jaswal, and E. Y. Tsymbal: *Phys. Rev. Lett.*, **95**, 216601 (2005).
3) S. Yuasa, A. Fukushima, H. Kubota, Y. Suzuki, and K. Ando: *Appl. Phys. Lett.*, **89**, 042505 (2006).
4) T. B. Massalski, H. Okamoto, P. R. Subramanian, and L. Kacprzak: *Binary Alloy Phase Diagrams* (ASM International, Ohio, 1990).
5) J. C. A. Huang, Y. M. Yu, C. C. Yu, C. H. Tsao, and C. H. Lee: *Phys. Rev. B*, **57**, 11517 (1998).
6) M. Ohtake, Y. Sato, J. Higuchi, and M. Futamoto: *J. Phys.: Conf. Ser.*, **266**, 012122 (2011).
7) J. Higuchi, M. Ohtake, Y. Sato, and M. Futamoto: *J. Phys.: Conf. Ser.*, **303**, 012053 (2011).
8) J. Higuchi, M. Ohtake, Y. Sato, F. Kirino, and M. Futamoto: *Thin Solid Films*, **519**, 8347 (2011).
9) M. Ohtake, T. Yanagawa, J. Higuchi, and M. Futamoto: *EPJ Web Conf.*, **40**, 08004 (2013).
10) P. Bayle-Guillemaud and J. Thibault: *Philos. Mag. A*, **77**, 475 (1998).
11) M. Ohtake, Y. Sato, J. Higuchi, T. Tanaka, F. Kirino, and M. Futamoto: *Jpn. J. Appl. Phys.*, **50**, 103001 (2011).
12) W. Tian, H. P. Sun, X. Q. Pan, J. H. Yu, M. Yeadon, C. B. Boothroyd, Y. P. Feng, R. A. Lukaszew, and R. Clarke: *Appl. Phys. Lett.*, **86**, 131915 (2005).
13) T. Tanaka, T. Nishiyama, K. Shikada, M. Ohtake, F. Kirino, and M. Futamoto: *J. Magn. Soc. Jpn.*, **34**, 21 (2010).
14) J. Higuchi, M. Ohtake, Y. Sato, T. Nishiyama, and M. Futamoto: *Jpn. J. Appl. Phys.*, **50**, 063001 (2011).
15) G. Wasserman: *Arch. Eisenhüttenwesen*, **16**, 647 (1933).
16) Z. Nishiyama: *Sci. Tohoku Univ.*, **23**, 638 (1934).
17) G. Kurdjumov and G. Sachs: *Z. Phys.*, **64**, 325 (1930).
18) T. Soda, S. Minakawa, M. Ohtake, M. Futamoto, and N. Inaba: *IEEE Trans. Magn.*, **51**, 2000904 (2015).
19) H. Shoji: *Z. Kristallogr.*, **84**, 74 (1932).
20) Z. Nishiyama: *Sci. Rep. Res. Inst. Tohoku Univ. A*, **25**, 76 (1936).

Received Mar. 7, 2015; Accepted May 26, 2016

Journal of the Magnetics Society of Japan

Vol. 40 No. 5 (通巻第 287号) 2016 年 9 月 1 日発行

Vol. 40 No. 5 Published Sep 1, 2016

by the Magnetics Society of Japan
Tokyo YWCA building Rm207, 1–8–11 Kanda surugadai, Chiyoda-ku, Tokyo 101–0062
Tel. +81–3–5281–0106 Fax. +81–3–5281–0107

Printed by JP Corporation Co., Ltd.
2–3–36, Minamikase, Saiwai-ku, Kanagawa 212–0055
Advertising agency: Kagaku Gijutsu-sha

発行：（公社）日本磁気学会 101–0062 東京都千代田区神田駿河台 1–8–11 東京YWCA会館 207 号室
製本：（株）ジェイピーコーポレーション 212–0055 神奈川県川崎市幸区南加瀬 2–3–36 Tel.（044）571–5815
広告取扱い：科学技術社 111–0052 東京都台東区柳橋 2–10–8 武田ビル 4F Tel.（03）5809–1132